THE RESIDENCE OF URANIUM IN ROLL FRONT DEPOSITS: A CASE STUDY

by

Timothy Orion Wyatt

A thesis submitted to the Faculty and the Board of Trustees of the Colorado School of

Mines in partial fulfillment of the requirements for the degree of Master of Science (Geology).

Golden, Colorado

Date _____

                                                Signed: _____
                                                            Timothy O. Wyatt

                                                Signed: _____
                                                      Dr. Katharina Pfaff
                                                          Thesis Advisor

Golden, Colorado

Date _____

                                                Signed: _____
                                                      Dr. Steven Enders
                                                  Professor and Department Head
                                                  Geology and Geological Engineering

ABSTRACT

Despite generally low uranium grades, roll-front uranium deposits are attractive exploration targets as these deposits are amenable to in-situ leaching (ISL) techniques. At the Lost Creek Project, a currently operating uranium mine in Wyoming, head grades were five times higher than pre-operational estimates. Similar mines, such as the Crow Butte mine in Nebraska, have experienced head grades that are in good agreement with pre-operational estimates. Ore samples from the Lost Creek Project and the Three Crow Expansion Area, a satellite deposit to the Crow Butte mine, were analyzed in order to understand their mineralogy and to understand the discrepancy between head grades and pre-operational estimates at the Lost Creek Project.

Fission track mapping, quantitative trace element mapping of selected areas using EPMA and high-resolution BSE imaging revealed that the uranium phases at the Lost Creek Project are contained in small (<1 µm) wispy phases. Using SEM and TEM techniques, the U bearing phases were identified as a fine intergrowth of kaolinite with becquerelite $(Ca(UO_2)_6O_4(OH)_6 \cdot 8(H_2O))$ and uranophane $(Ca(H_3O)_2(UO_2)_2(SiO_4)_2 \cdot 3H_2O)$. Initial head grades at Lost Creek of 211 ppm are in good agreement with solubility experiments for highly soluble becquerelite (250 ppm), whereas uranophane solubility peaks at 75 ppm in a bicarbonate concentration of $2.0x10^{-2}$ mol/L, which is in good agreement with bicarbonate concentrations used at the Lost Creek Project and with current head grades of 42 ppm. The large discrepancy of estimates and initial head grades at the Lost Creek Project is partly due to the different gamma ray intensity of uranophane versus primary U ore minerals usually found in U roll-front deposits. Uranophane has a gamma ray response of almost half of both uraninite and coffinite leading to an underestimated resource estimate. Moreover, the mobile nature of the U^{6+} ion allowed uranium mineralization of secondary minerals to occur away from the primary ore zone leading to a less well defined, larger ore zone.

Ore mineralogy at the Three Crow Expansion area was identified to be primarily coffinite $(U(SiO_4)_{1-x}(OH)_{4x})$ and is in good agreement with previous work and the ore mineralogy at the Crow Butte mine. In contrast, the Lost Creek Project is highly oxidized and primary U ore minerals have been replaced by secondary becquerelite and uranophane.

TABLE OF CONTENTS

LIST OF FIGURES

vii

LIST OF TABLES

ACKNOWLEDGEMENTS

CHAPTER 1

INTRODUCTION

1.1 Uranium

Uranium, the 92nd element on the periodic table, is born in violent supernovas during the death of a star. The debris from this event later formed our solar system and contributed uranium to the earth. Uranium was first discovered by Martin Klaproth, a German chemist, in 1789. Prior to the discovery of uranium's radioactive properties, uranium was mainly used as a coloring agent to give ceramics a yellowish glaze. Since Henri Becquerel's discovery of uranium's radioactive properties in 1896, the element has been used largely for military purposes and energy generation.

The average crustal abundance of uranium is 2.8 ppm (WNA, 2016), much too low to be economically mined. Therefore, concentration of uranium must occur to enrich grades to become economical. Due to the large ionic radius and high valence state, uranium is strongly incompatible and is not incorporated into the main rock forming silicates. During partial melting and crystal fractionation, uranium is preferentially concentrated in the silicate melts (Cuney, 2009). Consequently, the sources of uranium in ore deposits are often granites, rhyolites and tuffs (Cuney, 2009). The average granitoid contains 3-4 ppm uranium which is incorporated into the structure of stable accessory minerals (e.g. zircons, apatites, monazites; Cuney, 2009). Three "fertile granites" with U concentrations above the Clarke value (2.8 ppm) were identified: peralkaline, metaluminous, and peraluminous igneous rocks (Cuney, 2014). To yield U in economic concentrations, further concentration of uranium through ore forming processes must occur.

1.2 Overview of uranium deposits

Different classifications for uranium deposits have been presented throughout the years. Based on composition and origin of mineralizing fluids (Skirrow et al., 2009), on the time stratigraphic relationship of host rock to ore emplacement (Dahlkamp, 1978) and on the formation conditions throughout the geologic cycle (Cuney, 2009). In Cuney (2009), uranium deposits are sorted into a total of 6 categories and include deposits related to surface processes,

synsedimentary deposits, deposits related to hydrothermal processes, vein type deposits, deposits related to partial melting, and deposits related to crystal fractionation.

The most significant deposit type related to surficial processes are roll front deposits. Roll front deposits occur when uranium rich source rocks, commonly volcanic tuffs and U-rich granites, are leached by oxidized, meteoric water which transports the uranium down the hydraulic gradient until it encounters reducing conditions and precipitates uranium minerals in C", or roll-shaped ore zones at the redox interface. Common reductants include carbonaceous matter, sulfides, hydrocarbons and H_2S. Examples of roll front uranium mines include Smith-Ranch Highlands and Crow Butte in the United States.

The second category is the synsedimentary uranium deposits which include U-rich black shales and phosphorites. Phosphorites develop along shallow continental shelves with limited circulation. Phosphorites are common along the southern margin of the Tethys Ocean including Morocco which owns 75% of the world's phosphorites (Cuney, 2009). U-rich black shales occur in shallow marine environments with limited sediment input and abundant seawater circulation. Uranium is absorbed from seawater onto organic material and clays. Examples of U-rich black shales include shales near Ranstad, Sweden and Ronneburg-Gera, Germany.

Uranium deposits related to hydrothermal processes is the broadest category of U deposits. Included in this category are basal-type deposits, tabular deposits, roll front deposits, tectonic-lithologic deposits, solution-collapse breccia pipes, unconformity related deposits, synmetamorphic, metasomatic deposits, and uranium bearing skarns (Cuney, 2009). These deposits are generally epigenetic and form during fluid circulation in a wide variety of rock types. Mineralizing fluids can be meteoric, diagenetic, and metamorphic in origin. Unconformity-related deposits are diagenetic-hydrothermal uranium deposits. Unconformity deposits occur at the strong redox interface between thick sandstone deposits (oxidized) from above and crystalline basement (reduced) below where graphite-rich faults were reactivated. Factors influencing the formation of unconformity related deposits are the hot, oxidized, Ca-rich brine which dissolved uranium bearing minerals and void space created by reverse tectonics and quartz dissolution (Cuney, 2009). Tabular deposits often from in sandstone lithologies between impermeable clay layers. Uranium precipitation can occur either synsedimentary or, more commonly, during diagenesis. U is sourced from U-rich tuffs or possibly from brines expelled by underlying evaporitic sediments.

Vein type deposits occur in variety of lithologies including granites and volcanics. These deposits are generally relatively small with the exception of the Olympic Dam deposit in Australia. Granite related vein type deposits occur when oxidized, meteoric fluids leaching uraninite from granite mix with fluids from an overlying basing with enough reductants to precipitate uranium. The classic example is the mid-European Variscan uranium province which extends over 2000 km (Cuney, 2009). Volcanic related uranium deposits occur in calderas filled with felsic and mafic volcanic rocks. U can be sourced from U-rich peralkaline rhyolites and subalkaline granites. Larger deposits form where long-lived, shallow magma chambers exists that drive fluid convection over long periods of time. The Olympic Dam deposit is an IOCG deposit that is currently mined for Cu, Au, and U. The Olympic Dam deposit formed 1.6 Ga when magmatic activity, brecciation, and mineralization occurred during the emplacement of the Roxby Down granite (Pollard, 2006). Uranium precipitation occurred when hot, saline brines from felsic magma mixed with oxidized, meteoric water.

Partial melting related deposits occur when continental shelf deposits are metamorphosed to upper amphibolite facies and experience partial melting (Cuney, 2009). Mineralization is a result of either extreme fractionation of deeper granite bodies or from partial melting of U-rich metamorphic rocks. Crystallized uraninite from magma is the primary source of uranium, but U enrichment also occurs from magmatic fluids and supergene processes. In the Rössing uranium deposit located in Namibia, primary mineralization of uranium is dominantly uraninite with lesser amounts of betafite, $(Ca,U)_2(Ti,Nb,Ta)_2O_6(OH)$ and occurs in alaskites (Berning et al., 1976).

Crystal fractionation related deposits only occur in peralkaline complexes. High solubilities of U, Th, Zr, and REE result in a continual enrichment during magmatic fractionation, resulting in complex minerals containing abundant uranium. These deposits are rarely mined due to their complex and refractory nature. The Kvanefjeld deposit, located on the southwest coast of Greenland, is the largest deposit related to crystal fractionation. Uranium mineralization is in the form of steenstrupine, a U-Th-REE silicophosphate, hosted in lujavrite, a mafic nepheline-analcime syenite (Sørensen et al., 1974; Nielsen & Steenfelt, 1979).

1.3　In-situ leaching (ISL)

In-situ mining is the process of extracting minerals from the earth by dissolving them in a solution known as a lixiviant and pumping the pregnant solution to the surface where the minerals can be recovered. With this mining technique, there is minimal surface disturbance and no tailings or waste is being produced. A series of injection and production wells are positioned over the ore zone in a pattern. A specialized, oxygenated fluid, known as lixiviant, is then forced down the injection wells where it dissolves uranium ore and is subsequently removed from the subsurface through extraction wells (Fig. 1.1). In a processing facility, the pregnant solution is being treated and the uranium recovered through resin/polymer ion exchange or solvent extraction to produce U_3O_8, or yellowcake, a fuel used in nuclear reactors.

In-situ leaching (ISL) operations accounted for 48% of total uranium production (29,197 tons of uranium) in 2015 which accounts for most of the uranium production in the United States, Kazakhstan, and Uzbekistan (WNA, 2016). ISL operations are also currently producing in Australia, China and Russia.

The geometry of injection and extraction wells (quadrilateral or hexagonal pattern) depends on the nature of the ore body. Additional monitoring wells are drilled surrounding the operation to ensure that uranium is not mobilized outside of the mining area.

Lixiviant chemistry can vary depending on the characteristics of the host rock and ore mineralogy. There are two types of lixiviants: acidic and alkaline solutions. Acidic lixiviants are prohibited in the United States, but are widely used in Kazakhstan and Australia using sulfuric acid as an oxidant to dissolve uranium. Acidic lixiviants are only effective in host rock that contains less than 2.0% carbonates, work faster and achieve greater uranium recoveries rates of up to 90% compared to alkaline lixiviants (up to 70% recovery; WNA, 2016).

In-situ mining has multiple benefits over traditional mining. Surface disturbance is minimal and ISL operations don't produce any tailing or waste rock. Air quality at ISL sites is much better compared to conventional mine sites due to the lack of heavy equipment and waste dumps which can release U-bearing dust into the air. ISL mines are more economic due to the limited infrastructure required and fewer employees needed.
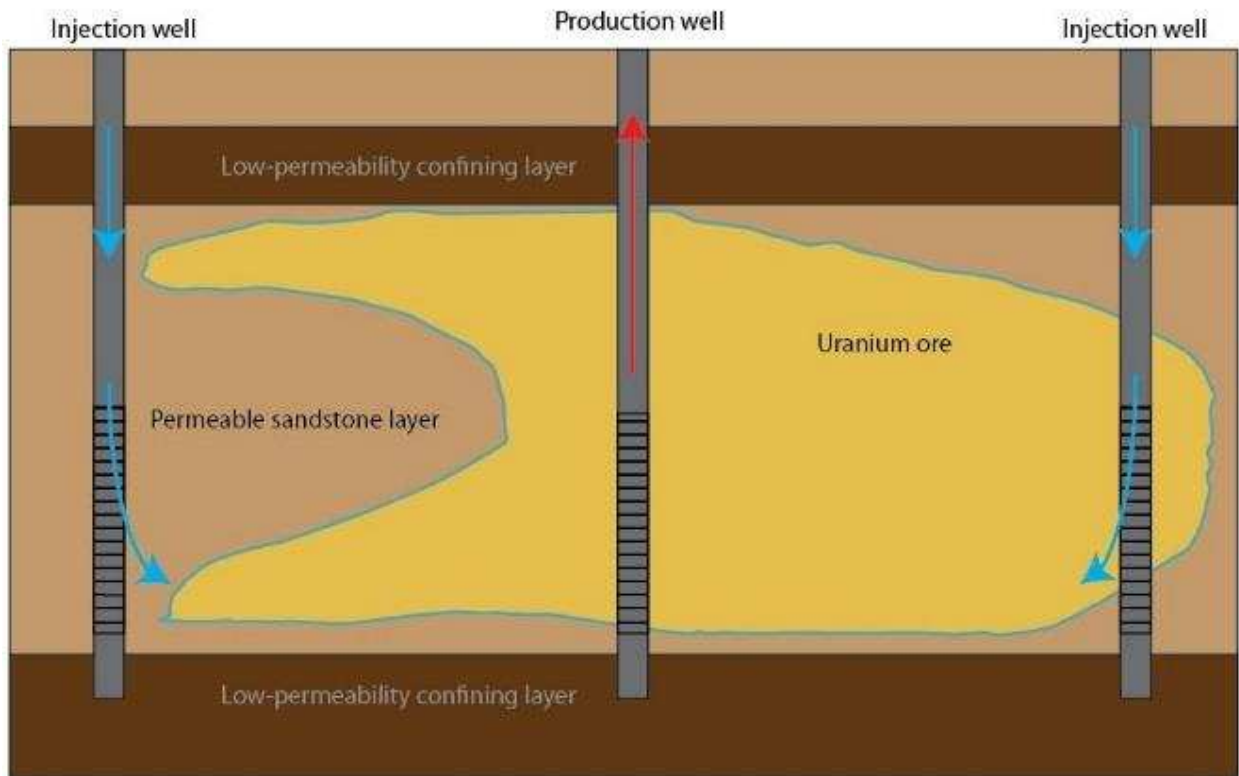
Figure 1.1 Schematic of in-situ leaching (ISL). A lixiviant is forced down an injection well where it dissolves uranium in the roll front. The pregnant solution is then extracted through a production well where it is sent to processing to produce yellowcake.

1.4 Fission track mapping

Radioactivity was first discovered in 1896 by Henri Becquerel when he discovered that photographic plates could be 'developed' using potassium uranyl sulfate (Martins, 1997). The photographic plate was left in contact with the potassium uranyl sulfate which left the plate fogged from exposure to radiation. The principals of fission track mapping are very similar.

Fission track mapping is a method that creates a distribution map of radioactive elements within a sample (especially highly fissionable uranium and plutonium). A detector slide is placed over the uranium-bearing sample and left in a nuclear reactor to induce fission within the U^{235} isotope. Once U^{235} has been exposed to a thermal neutron, fission is induced resulting in fission fragments which damage the structure of the detector slide. The damage in the structure can be made visible by chemical etching using HF or NaOH. The detector slide can then be used as a map to identify high concentrations of uranium in the samples (Fig. 1.2).

Fission track mapping is a very useful tool to locate elevated uranium concentrations in samples from low grade deposits. A previous study conducted on the low-grade Three Crow uranium deposit conducted by Liebold (2007) did not find any U ore minerals due to their fine-grained nature. Using fission track mapping, areas with low-grade uranium can be identified much more readily. The fission track mapping technique provides much greater sensitivity and resolution than other techniques.
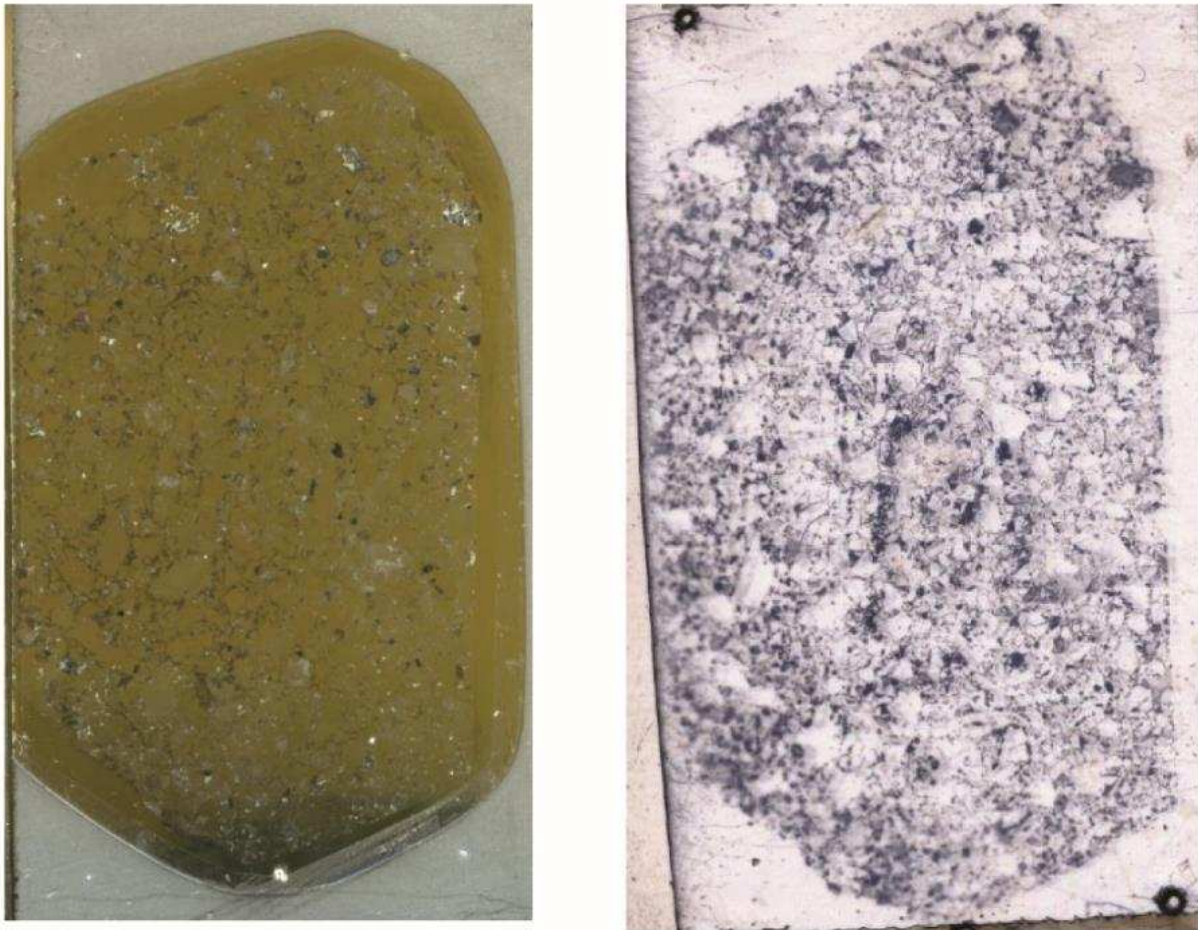
Figure 1.2 Fission track mapping induces the fission of uranium in the thin section (left) and produces a uranium distribution map (right). Sample 11C: 446-447 shown in photo.

CHAPTER 2

THE RESIDENCE OF URANIUM IN ROLL FRONT DEPOSITS: A CASE STUDY

2.1   Abstract

Despite generally low uranium grades, roll-front uranium deposits are attractive exploration targets as these deposits are amenable to in-situ leaching (ISL) techniques. At the Lost Creek Project, a currently operating uranium mine in Wyoming, head grades were five times higher than pre-operational estimates. Similar mines, such as the Crow Butte mine in Nebraska, have experienced head grades that are in good agreement with initial estimates. Ore samples from the Lost Creek Project and the Three Crow Expansion Area, a satellite deposit to the Crow Butte mine, were analyzed in order to understand their mineralogy and to understand the discrepancy between head grades and pre-operational estimates at the Lost Creek Project.

Fission track mapping, quantitative trace element mapping of selected areas using EPMA and high-resolution BSE imaging revealed that the uranium phases at the Lost Creek Project are contained in small (<1 µm) wispy phases. Using SEM and TEM techniques, the U bearing phases were identified as a fine intergrowth of kaolinite with becquerelite $(Ca(UO_2)_6O_4(OH)_6 \cdot 8(H_2O))$ and uranophane $(Ca(H_3O)_2(UO_2)_2(SiO_4)_2 \cdot 3H_2O)$. Initial head grades at Lost Creek of 211 ppm are in good agreement with solubility experiments for highly soluble becquerelite (250 ppm), whereas uranophane solubility peaks at 75 ppm in a bicarbonate concentration of 2.0×10^{-2} mol/L, which is in good agreement with bicarbonate concentrations used at the Lost Creek Project and with current head grades of 42 ppm. The large discrepancy of estimates and initial head grades at the Lost Creek Project is partly due to the different gamma ray intensity of uranophane versus primary U ore minerals usually found in U roll-front deposits. Uranophane has a gamma ray response of almost half of both uraninite and coffinite leading to an underestimated resource estimate. Moreover, the mobile nature of the U^{6+} ion allowed uranium mineralization of secondary minerals to occur away from the primary ore zone leading to a less well defined, larger ore zone.

Ore mineralogy at the Three Crow Expansion area was identified to be primarily coffinite $(U(SiO_4)_{1-x}(OH)_{4x})$ and is in good agreement with previous work and the ore mineralogy at the

Crow Butte mine. In contrast, the Lost Creek Project is highly oxidized and primary U ore minerals have been replaced by secondary becqurelite and uranophane.

2.1 Introduction

Roll front uranium deposits are sedimentary-hosted uranium deposits often occurring in intramontane basins proximal to exposed uraniferous granites. Host rocks are permeable and porous sandstone aquifers which are poorly cemented and bounded by low permeability, fine-grained sedimentary units (e.g. siltstones; Fig. 2.1). The uranium is sourced from a combination of granites and tuffs (Harshman & Adams, 1980). Uranium in the oxidized, hexavalent state (U^{6+}), is readily dissolved and highly mobile while uranium in the reduced, tetravalent state (U^{4+}) is much more stable. Oxidized, meteoric waters scavenge uranium from tuffs and granites and, driven by the hydraulic gradient, transport the uranium towards the center of the basin. Once the uranium encounters reducing conditions, U^{6+} is reduced to the immobile U^{4+} and precipitates as primary uranium minerals. According to the literature, the dominant species in most roll front deposits is either coffinite ($U(SiO_4)_{1-x}(OH)_{4x}$) or uraninite (UO_2) (Stewart et al., 1999) or the secondary minerals carnotite ($K_2(UO_2)_2(VO_4)_2 \cdot 3H_2O$) and tyuyamunite ($Ca(UO_2)_2V_2O_8 \cdot (5-8)H_2O$) (Adler & Sharp, 1967). The uranium is deposited at the redox boundary which forms a C-shaped deposit in cross-section otherwise known as a "roll" (Fig. 2.1). Uranium concentrations vary within the roll, with (1) higher concentrations on the concave side of the roll, (2) decreased concentrations in the oxidized rock near the concave boundary, and (3) concentrations decreasing toward the convex boundary in reduced rock (Harris, 1984). In map view, rolls form a sinuous pattern following the redox boundary which is controlled by the flow of groundwater (Fig. 2.2).

Roll front uranium deposits are becoming increasingly attractive deposits due to their amenability to in-situ leaching (ISL). ISL mines operate with a series of injection and production wells and thus have minimal surface disturbance, produce no tailings, and are much more economical to mine than traditional methods such as open pits and underground mines.

A solution of sodium bicarbonate ($NaHCO_3$) in oxygenated water (known as a lixiviant) is pumped through injection wells and into the uranium-bearing rock where it dissolves uranium (Ur-Energy Inc., 2016). The lixiviant, now containing uranium in ppm levels, is then pumped out
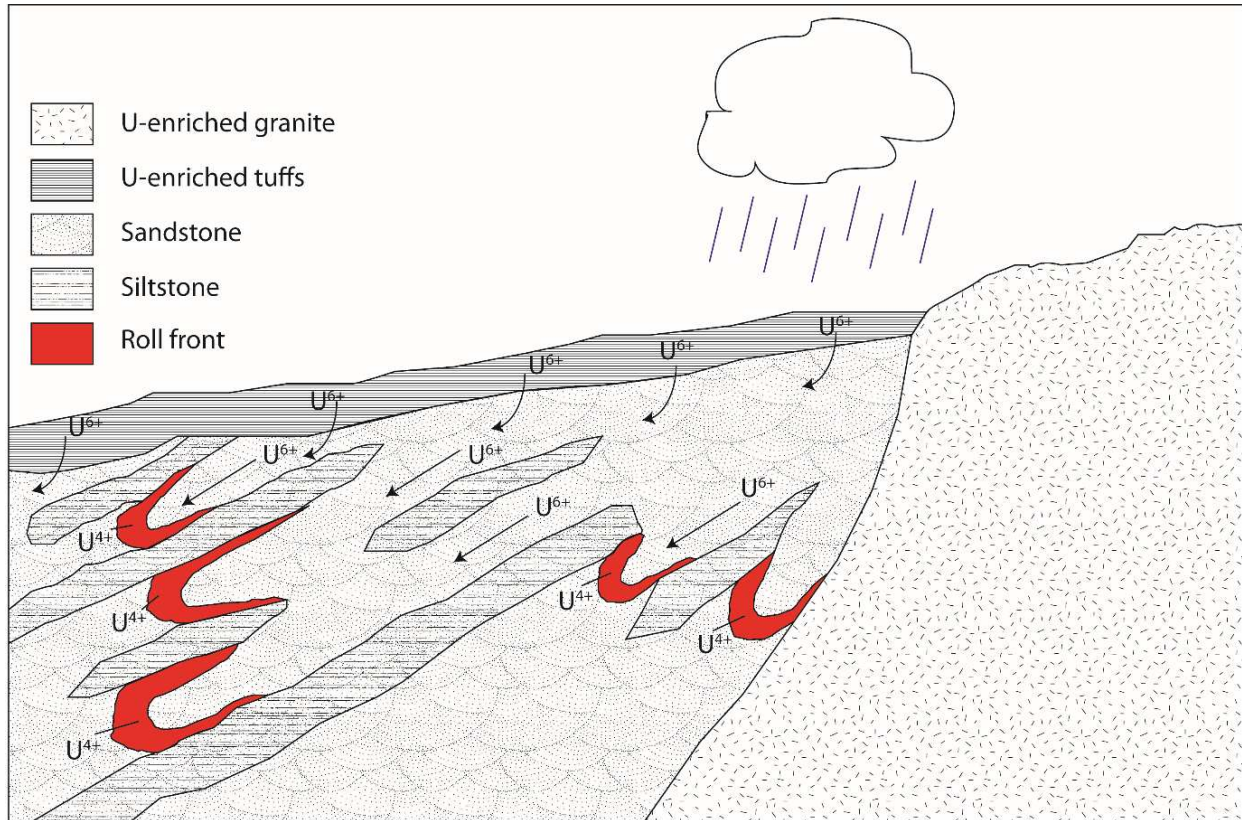
Figure 2.1 Model for the genesis of uranium roll fronts. Granites and tuffs enriched in uranium are leached by oxidizing meteoric water. Uranium in the 6+ oxidation state is much more mobile and are transported towards the center of the basin. When the groundwater intersects reducing conditions, the uranium is reduced to the 4+ oxidation state and precipitates into C-shaped rolls.

of the formation through production wells and is piped to a nearby processing plant that extracts the uranium and produces yellowcake (U_3O_8) using resin/polymer ion exchange or solvent extraction (Ur-Energy Inc., 2016).

Pre-operational estimates of uranium content in pregnant solutions at the Lost Creek Project, an actively mined roll front in southern Wyoming, were placed at 42 ppm U (Fig. 2.3), however, when the Lost Creek Project began production in late 2013, the pregnant solution contained 211 ppm U, more than 5 times pre-operational estimates (Ur-Energy, 2016). After three years of production in late 2016, the U in pregnant solution has decreased to 39 ppm, approximately the original expected head grades. The Three Crow Expansion Area (TCEA), a satellite deposit of the Crow Butte uranium mine (operating since 1991), is a pre-operational
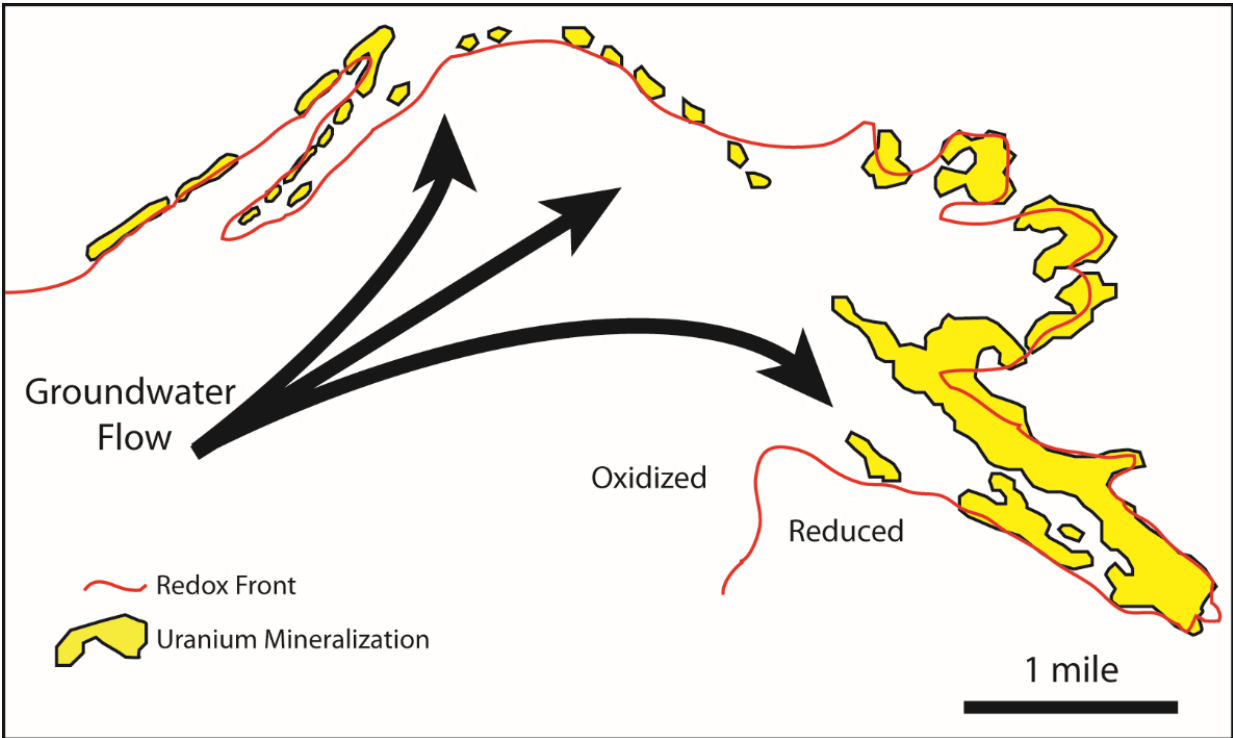
Figure 2.2 Map view of the distribution of uranium mineralized zones (modified from Dahl & Hagmaier, 1976).

deposit located in the Crawford Basin in northwestern Nebraska. Previous studies by Liebold (2007) characterized the differences in geochemistry and mineralogy of the alteration halo of the TCEA, however, the U ore mineral could not be identified.

The aim of this project is to characterize the uranium ore present at the Lost Creek Project and the Three Crow Expansion Area (TCEA), to understand why estimates and initial head grades were hugely discrepant at the Lost Creek Project and to increase our understanding of roll front deposits. Multiple analytical methods have been used at a progressively higher resolution and include (in increasingly higher resolution) optical mineralogy, fission track mapping, automated mineralogy, electron probe microanalysis (EPMA), field-emission scanning electron microscopy (FE-SEM), and transmitted electron microscopy.
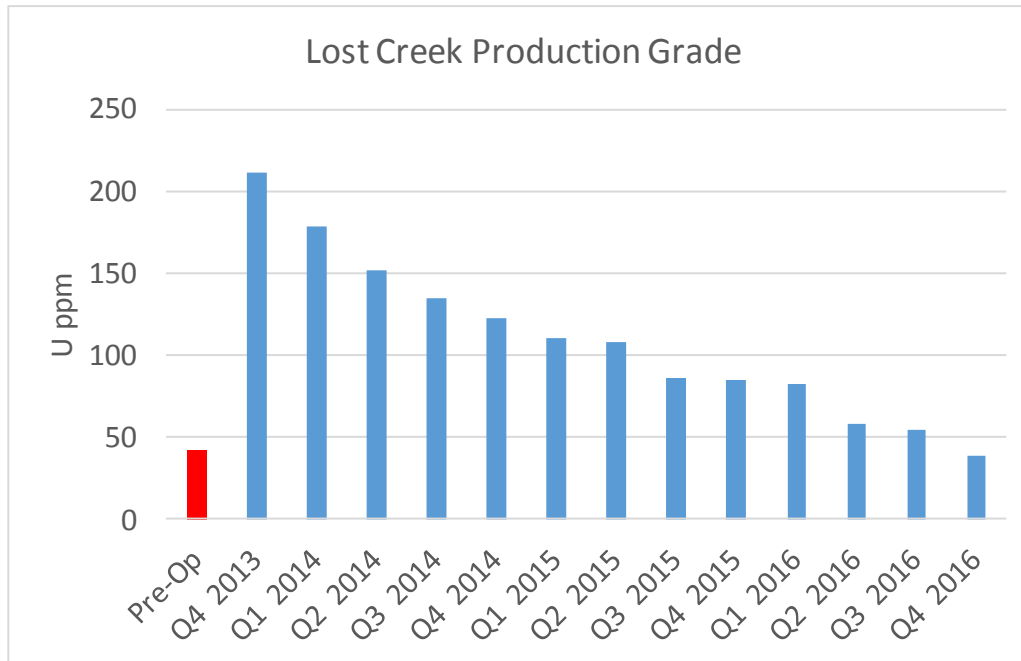
Figure 2.3 U concentration in pregnant solutions from the Lost Creek Project. In pre-operational estimates, U in solution was expected to be 42 ppm U. Initial head grades in the 4th quarter of 2013 contained 211 ppm U, over 5 times the pre-operational estimates.

2.2   Geologic Background

The following section will cover the geological features of the Lost Creek Project and the Three Crow Expansion Area including the location, stratigraphy and measured, indicated, and inferred resources.

2.2.1   Lost Creek Project

The Lost Creek Project is a currently operating ISL mine located in Sweetwater County, south-central Wyoming (Fig. 2.4). The Lost Creek Project is located in the Great Divide Basin (GDB), an oval shaped intramontane basin that covers an area of over 9000 km^2 (Ur-Energy, 2016). The Great Divide Basin is bounded to the north by the Wind River Range and Granite Mountains, on the west by the Rock Springs Uplift, on the south by the Wamsutter Arch and to the east by the Rawlins Uplift. In the northeast section of the Great Divide Basin where the Lost

Creek Project lies, the basin is filled with up to 7620 meters of sediment (Ur-Energy, 2016). At the Lost Creek Project, indicated and measured resources total 1.038 million kg U_3O_8 with an additional 0.227 million kg of inferred resources (Ur-Energy, 2016). The mine has produced 635,000 kg U_3O_8 as of September 2015 (Ur-Energy, 2016).

In addition to the Lost Creek Project, Ur-Energy Inc. has multiple permit areas that contain satellite deposits nearby, including the LC North, LC West, LC East, and LC South, all of which occur in the Battle Springs Formation (Fig. 2.5). The Battle Springs Formation at the Lost Creek Property can be divided into two units: Member A and Member B (Stephens, 1964). Member A is at least 670 m thick and composed of three major rock types, and, in descending order of abundance, are conglomeratic arkose, cobble and boulder conglomerates, and carbonaceous siltstone (Stephens, 1964). The conglomeratic arkose demonstrates cross-bedding indicative of fluvial deposition with alternating fine- and coarse-grained layers (Stephens, 1964). This unit is composed of poorly sorted, angular quartz, weathered feldspar and micas with granite pebbles scattered throughout (Stephens, 1964). Cobble and boulder conglomerates occur

Figure 2.4. Regional map of the Lost Creek Project and the Three Crow Expansion Area.

as lenses with increasing clast size (~15 cm near the base and 30 cm at the top) and abundance towards the top of Member A (Stephens, 1964). The composition of cobbles and boulders is predominantly granite that is similar to exposures in the Granite Mountains. The carbonaceous siltstones of the Battle Springs Formation generally are less than 1m in thickness and composed of a sandy siltstone with grains of quartz, feldspar, and rock fragments (Stephens, 1964).

The bottoms of the siltstone units are marked by a sharp contact, while the upper contacts are much more gradational. The siltstones contain abundant carbonaceous material, predominantly lignites and poorly preserved plant fossils. The siltstones are of economic importance, as uranium appears to be localized proximally (Stephens, 1964). Member B is composed of a sequence of conglomeratic arkose and giant boulder conglomerate and sits above Member A (Stephens, 1964). The thickness is quite variable, due to an unconformity marking the base of the member and an erosional surface at the top, ranging from 150-750 m with an unconformity at the base and an erosional surface at the top (Stephens, 1964). The paleoenvironment of the host rocks was a high-energy fluvial environment, most likely proximal to the Granite Mountains that were deposited in an alluvial fan. Meandering streams were present, evidenced by channels with boulders directly buried under fine-grained material and abundant carbonaceous material (Stephens, 1964). The giant boulder conglomerate was most likely a results of a steep fault escarpment as the Granite Mountains were thrust up relative to the basin (Stephens, 1964).

Within the property, the Battle Springs Formation is composed of 60-80% of poorly consolidated, medium to coarse grained arkosic sandstones that are less than 15 m in thickness (Ur-Energy, 2016). The remaining 20-40% consists of fine grained sedimentary units up to 8 m in thickness.

To the west of the Lost Creek Project, the Battle Springs Formation interfingers with the Green River and Wasatch Formations (Fig. 2.5), also Eocene in age. The Green River Formation was formed in a combination of lacustrial and playa paleoenvironments and is composed of three members: the Luman, Tipton Shale, and the Laney Shale with maximum thicknesses of 80, 85, and 200 m (Fig. 2.5; Eugster & Hardie, 1975; Pipiringos, 1955). The Luman Member is a sequence of oil shales, calcareous sandstones, varved siltstone and shale and is underlain by the Red Desert Member and overlain by the Niland Member (Fig. 2.5; Pipiringos, 1955). The Tipton Shale Member is composed of highly organic dolomitic shales and oil shales and sits between

the older Niland Member and the younger Cathedral Bluffs Member (Fig. 2.5; Eugster & Surdam, 1973). The final unit in the Green River Formation, the Laney member, contains sediments of dolomitic mudstones, limestones, sandstones, siltstones, and oil shales (Pipiringos, 1955). The Wasatch Formation is composed of three units: the Red Desert Member, the Niland Member, and the Cathedral Bluffs Member (Pipiringos, 1955). The Red Desert Member is a sequence of coal beds, shales, siltstone, and biotitic sandstones (Pipiringos, 1955) and reaches a maximum thickness of 300 m. The Red Desert is underlain by the Fort Union Formation and overlain by the Luman Member (Fig. 2.5). The Niland Member is only 120 m thick and is composed of a sequence of coal beds, shales, siltstone, and sandstone (Pipiringos, 1955). It sits upon the Luman Member and below the Tipton Member (Fig. 2.5). The final member of the Wasatch Formation, the Catherdral Bluffs Member, is positioned in between the Tipton and
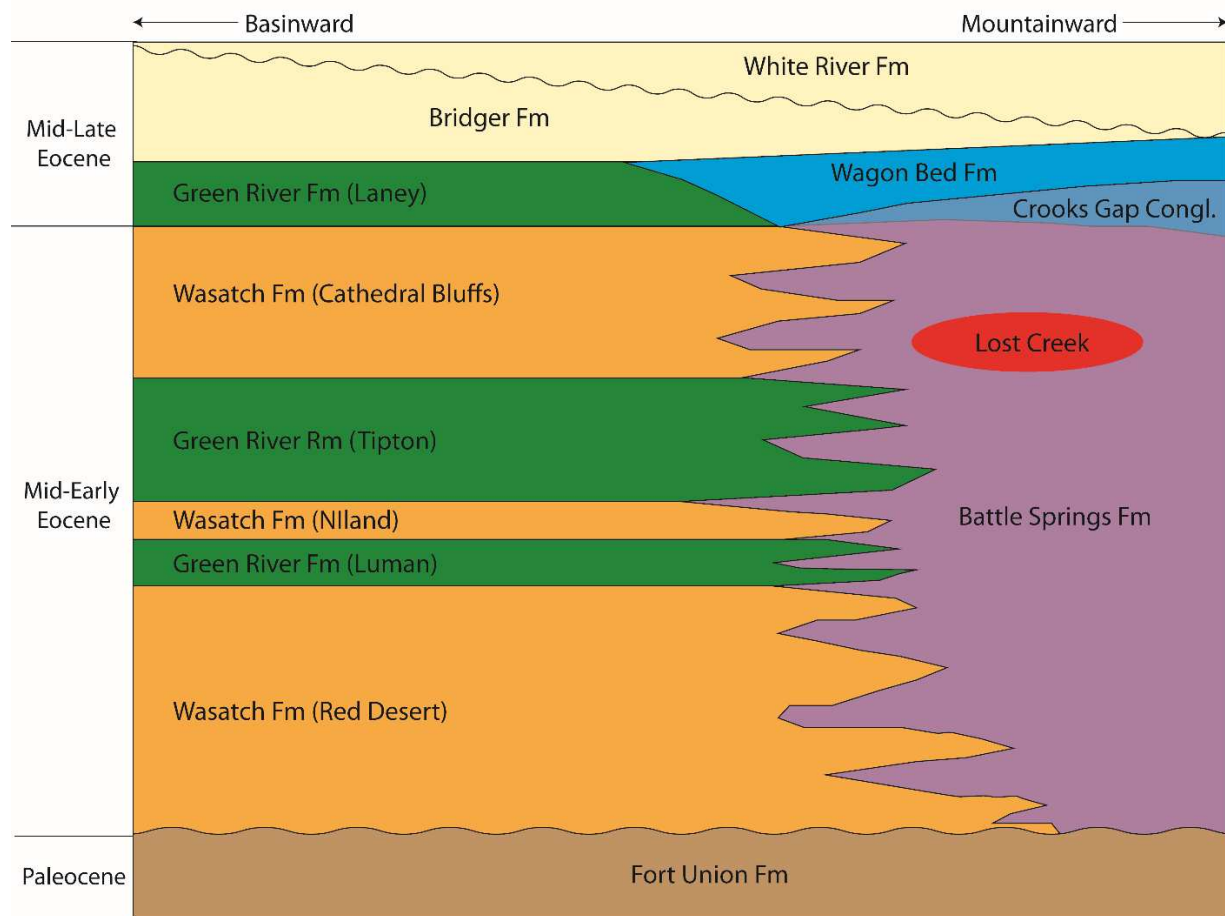
Figure 2.5 Stratigraphic section of the Great Divide Basin with the location of the Lost Creek Project ore zone circled in red (not to scale; modified from Ur-Energy Inc., 2016).

Laney Shale Members of the Green River Formation and is composed of a sequence of red and green claystones (Fig. 2.5). The Laney Shale Member reaches a maximum thickness of 275 m (Pipiringos, 1955).

2.2.2 Three Crow Expansion Area (TCEA)

The Three Crow Expansion Area (TCEA) is a pre-operational deposit located in the Crawford Basin in northwestern Nebraska (Fig. 2.4). It is a satellite deposit of the currently operating ISL Crow Butte roll-front deposit. The Crawford Basin is a sub-basin of the Denver Basin and encompasses an area of approximately 1000 km^2 (DeGraw, 1971). The Crawford Basin is dominantly composed of 3 formations (the Pierre Shale, the White River Formation and the Arikaree Group) underlain by pre-Cambrian granite (Fig. 2.6). The Pierre Shale is a dark-gray to black marine shale that was deposited during the late Cretaceous when the Interior Seaway of North America covered much of the Midwest of the United States. Thicknesses of the Pierre Shale in this region range from 360-460m (Gjelsteen & Collings, 1988). The top of the Pierre Shale is composed of a deeply weathered soil horizon, brownish to yellow in color that is up to 9m thick and marks an erosional unconformity (Ferret Exploration Company of Nebraska Inc., 1987; Fig. 2.6). The unit overlying the Pierre Shale is the White River Group, which was deposited in fluvial, lacustrine and eolian environments (Crow Butte Resources, Inc., 2010). The White River Group is composed of three different formations (from oldest to youngest): the Chamberlain Pass Formation, the Chadron Formation, and the Brule Formation (Fig. 2.6). The Chamberlain Pass Formation, also known as the Basal Chadron Sandstone (Gjelsteen & Collings, 1988), overlies the Pierre Shale and is composed of interbedded coarse-grained, cross-bedded, arkosic sandstones and thin silt and clay layers varying in thickness and lateral continuity with multiple thin lenses of gravel sized conglomerates. Sandstones are composed of 65% quartz, 25% feldspar and 10% rock fragments (Gjelsteen & Collings, 1988) with up to 30% air-fall ash (Singler & Picard, 1979). The sands are not well cemented with only minor amounts of calcite and silica cement. Thicknesses for this unit at the TCEA average 18m and range from 0 to 100m (Gjelsteen & Collings, 1988). Channel sandstones of the Chamberlain Pass Formation occupy a width of 24-32km and extend from Lusk, Wyoming to Crawford, Nebraska (Gjelsteen & Collings, 1988). Previous work (Seeland, 1985; Stanley, 1976) suggests that the sandstone is sourced from multiple locations including the Laramide Range, the Hartville Uplift and the

Black Hills. The depositional environment of this area was a high-energy braided stream environment which accounts for the low-energy overbank silt and clay lenses. Overlying the Chamberlain Pass Formation is the Chadron Formation, which is dominantly composed of fine-grained mudstones and claystones with occasional tabular and lenticular channel sandstones. Thickness is relatively uniform at 45m (Gjelsteen & Collings, 1988). Swinehart et al. (1985) suggests that the fine-grained units are reworked ash sourced from violent volcanism in the Basin and Range province (Chadwick, 1985). Thick layers of montmorillonite and kaolinite are present as a result of devitrification during diagenesis (Gjelsteen & Collings, 1988). The youngest formation of the White River Formation is the Brule Formation which ranges from 40-160m and is dominantly composed of siltstones and claystone sourced from volcaniclastic material (Gjelsteen & Collings, 1988). Sandstone-filled channels are uncommon in the lower Brule but are increasingly common towards the top of the formation.
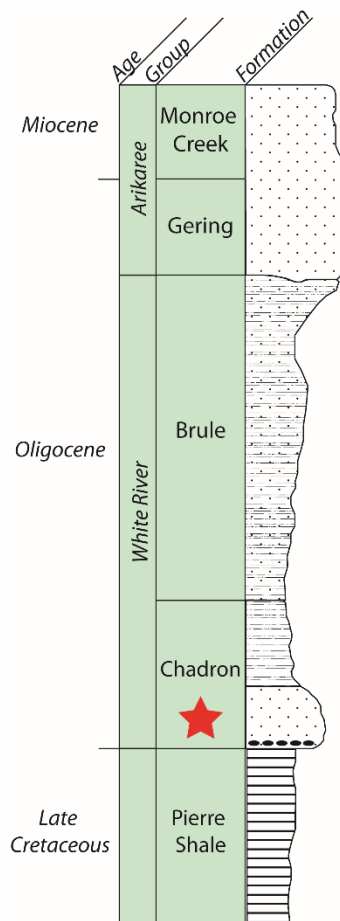
Figure 2.6. Stratigraphic section from the Crawford Basin (from Gjelsteen & Collings, 1988).

The Arikaree Group (Fig. 2.6) is variable in composition and contains calcareous cemented, cross-bedded sandstones, siltstones, carbonates and tuffaceous beds (Hoganson et al., 1998). The maximum thickness of the Arikaree Group in northwestern Nebraska is approximately 210m (MacFadden & Hunt, 1998). The Oligocene-Miocene aged Arikaree overlies the White River Group but is not always present within the Crawford Basin. At the Three Crow project, the White River Group is overlain by alluvium and the Arikaree Group is not present.

The surface expression of the proposed TCEA will encompass an area of approximately 665 hectares with the orebody occurring approximately 175-290 m below ground surface and the width of the orebody ranges from 640-1220 m. The TCEA has an indicated resource of approximately 1,701,190 kg U_3O_8 with an inferred resource of 515,032 kg. Total reserves are estimated to be 2,222,603 kg. Ore grades range from 0.05 to 0.5 wt. % U_3O_8 but average 0.22 wt. % U_3O_8. Estimated annual production is 272,155 kg (Crow Butte Resources Inc., 2010).

2.3   Analytical Methods

This section will explain the analytical methods employed in this research. Analytical techniques used in this study include optical microscopy, automated mineralogy, fission track mapping, electron probe microanalysis, backscattered electron imaging using a field emitter scanning electron microscope (FESEM), and transmitted electron microscopy (TEM).

2.3.1   Optical microscopy

Four thin sections were analyzed using optical microscopy, both transmitted (PPL and XPL) and reflected light to investigate the mineralogy of the samples examined.

2.3.2   Fission track mapping

Four thin sections, two from the Lost Creek Project and two from the TCEA, were overlain with relatively pure muscovite mica and inserted into the Training, Research, Isotopes, General Atomics (TRIGA) nuclear reactor located at the United States Geological Survey, Lakewood, Colorado. The samples and muscovite were then irradiated at a neutron flux of $2.0x10^{12}$ neutrons/cm^2/sec for approximately 8 hours. Structural damage resulting from the decay

of radioactive elements is recorded in the muscovite. The muscovite is then immersed in reagent grade hydrofluoric acid (58%) for 10 minutes to increase the visibility of structural damage and subsequently washed with water and alcohol. The final product is a qualitative map of uranium abundance in the thin section recorded on the muscovite sheet which is then mounted on a glass thin section in the same orientation for further analysis. Using an optical microscope, U-bearing areas can be identified by comparing the fission track map with the respective thin section. Navigation is accomplished by recognizing areas of little to absent fission tracks and comparing those to framework grains from the thin section, which are largely void of uranium bearing minerals (Zielinski, unpublished).

2.3.3   Automated Mineralogy

A total of four thin sections, 2 from the Lost Creek Project (11C: 446-447 and 13C: 412-413) and 2 from the TCEA (H161C-002F and H161C-W) were analyzed using automated scanning electron microscopy at the Colorado School of Mines. The samples were loaded into the TESCAN-VEGA-3 Model LMU VP-SEM platform and the analysis was initiated using the control program TIMA3. Four energy dispersive X-ray (EDX) spectrometers acquired spectra from each analysis point with a BSE brightness higher than 60% for uranium bright phase search scans and from every analysis point with a BSE brightness higher than 15% for high-resolution mineralogy maps (modal mode). A beam stepping interval (i.e. spacing between acquisition points) of 1 μm, an acceleration voltage of 25 keV and a beam intensity of 14 was chosen for analysis. Interactions between the beam and the sample were modeled through Monte Carlo simulation. The EDX spectra were compared with spectra held in a look-up table allowing an assignment to be made of a composition at each acquisition point. The assignment makes no distinction between mineral species and amorphous grains of similar composition. Results were output by the TIMA software as a spreadsheet giving the area percent of each composition in the look-up table. This procedure allows a compositional map to be generated. Composition assignments were grouped appropriately.

2.3.4 Electron probe microanalysis

Electron probe microanalysis (EPMA) was conducted on two thin sections from the Lost Creek Project. Areas were selected based on track density from the fission track maps. The analysis was performed at the United States Geological Survey Denver Microbeam Laboratory, Lakewood, Colorado with a JEOL 8900 electron probe microanalyzer. The analyses were conducted using a beam current of 100 nA and an acceleration voltage of 20 kV. A 1 µm step size was used with an acquisition time of 100 ms per pixel. Created maps were 512 x 512 µm. Analyzed elements in this analysis were U, Al, and Si. Standards used for calibration included UO_2 for U and the Miyake Anorthite for both Si and Al. Using the 3σ method with 99% confidence, uranium has a detection limit of 0.4 wt. %.

2.3.5 Field emission scanning electron microscopy

The JEOL 5800LV at the United States Geological Survey Denver Microbeam Laboratory and the TESCAN Mira3 LMH Schottky field emission-scanning electron microscope, equipped with a Bruker XFlash® 6/30 silicon drift detector for energy-dispersive X-ray spectrometry (EDS) at the Colorado School of Mines were employed for imaging and point analysis. Areas of interest were selected using the uranium maps produced by EPMA and automated mineralogy analysis.

2.3.6 Transmitted electron microscopy

Specimens were prepared with the FEI Co. Helios 600i dual column Focused Ion Beam (FIB) creating a 12 µm x 12 µm area with a thickness of ~100 nm. A ~2 µm thick layer of platinum was deposited on the liftout prior to cutting using the ion beam to protect the specimen from damage. A U-cut is incised around the specimen and a manipulator probe is inserted and secured to the specimen using platinum GIS deposition. The specimen is then extracted from the bulk sample and secured to a copper grid again using platinum GIS deposition. The manipulator is then separated from the specimen using ion milling.

To obtain crystallographic and compositional information, the FEI Talos F200X CTEM/STEM at the Electron Microscopy Laboratory at the Colorado School of Mines was used at an acceleration voltage of 200 keV. Bright field images were acquired using a variety of

19

imaging conditions, and electron diffraction patterns were acquired using a camera length of 410 mm. STEM-EDS spectral images were acquired using 4 windowless detectors at 150 kcps simultaneously with high-angle annular dark field (HAADF) information. Quantitative sodium, calcium, uranium, silicon, and aluminum elemental maps were generated using Bruker ESPRIT software and Cliff-Lorimer ratio routines. In addition to maps, line scans and point analyses were also generated.

2.4   Results

The following section will include selected results from the multiple analyses. For the complete set of results, see Appendix A.

2.4.1   Optical microscopy

Thin sections from the Lost Creek Project (samples 450C: 434-435 and 8C: 433-434) and the Three Crow Expansion Area (samples H161C-002F and H-161C-W) were analyzed using transmitted and reflected light (PPL and XPL).

2.4.1.1 Lost Creek

Samples from the Lost Creek Project are composed of approximately 35% quartz, 25% alkali feldspar, 25% plagioclase feldspar, and 10% clay minerals, and the remaining 5% are represented by lithic fragments and accessory minerals which include minor amounts of biotite, chlorite, rutile, apatite, calcite and sulfides including galena and pyrite. The samples contain abundant pore space and where matrix is present, it is composed of fine grained clay minerals. Sample 8C: 433-434 is characterized by moderately sorted, sub-angular framework grains with the bulk of grain sizes between 500 and 1000 µm. Sample 450C: 434-435 is poorly sorted, with sub-rounded to sub-angular grains that are much coarser in size, ranging from 1-3 mm. No uranium minerals were identified using optical microscopy alone.

2.4.1.2 Three Crow

Samples from the TCEA are composed of more quartz than the samples from the Lost Creek Project with less feldspar and clays. The mineralogy of samples H161C-002F and H161C-

W includes 60-70% quartz, 10-20% orthoclase, and 10-20% plagioclase. Pyrite content is 1-3 area % in sample H-161C-W than in sample H161-002F which has less than 1%. The clay content of these samples is less than 1%. Like the Lost Creek Project samples, the rocks contain abundant pore space. Grains from both Three Crow samples are sub-rounded to rounded and are poorly sorted. The grain size in sample H-161C-W ranges from approximately 100-250 µm. Sample H-161C-002F has a bimodal grain size distribution with the smaller grain size fraction at 50 µm in size and the larger grain size at 500 µm in size. No uranium minerals were recognized using optical microscopy techniques.

2.4.2 Fission track mapping

Fission track mapping was conducted on a total of 4 thin sections: 2 from each the Lost Creek Project (13C: 412-413 and 11C: 446-447) and the TCEA (H161C-002F and H161C-W). The fission track maps highlight the areas containing uranium (Fig. 2.7A, 2.7C) that are found within the thin sections (Fig. 2.7B, 2.7D). Fission tracks are primarily concentrated in the fine-grained matrix. Concentration within the matrix is heterogeneous with some areas being completely saturated with fission tracks, while others are without. It is difficult to identify the boundaries of the uranium minerals with fission track mapping alone due to a saturation of fission tracks in areas containing abundant uranium, which obscures the extent of uranium mineralization. Although uranium mineralization is generally bound to clays, it occurs as small points sources in between tightly packed framework grains without any matrix in between (Figure 2.7C). Uranium is almost entirely absent within the framework grains, although zircons contained within quartz are a rare exception. Biotite is often a source of a moderate density of fission tracks within certain planes.

2.4.3   Electron microprobe analysis

A total of 14 areas from samples 11C: 446-447 and 13C: 412-413 from the Lost Creek Project were utilized to create false-colored uranium distribution maps (Figs. 2.8-2.9). Uranium concentrations in the mapped areas were quite variable ranging from <1.0 wt. % U to over 25.0 wt. % U. In the 14 areas selected for mapping, the majority of the uranium occurs in concentrations less than 3.0 wt. % U. These low-grade areas are associated with the matrix clays.
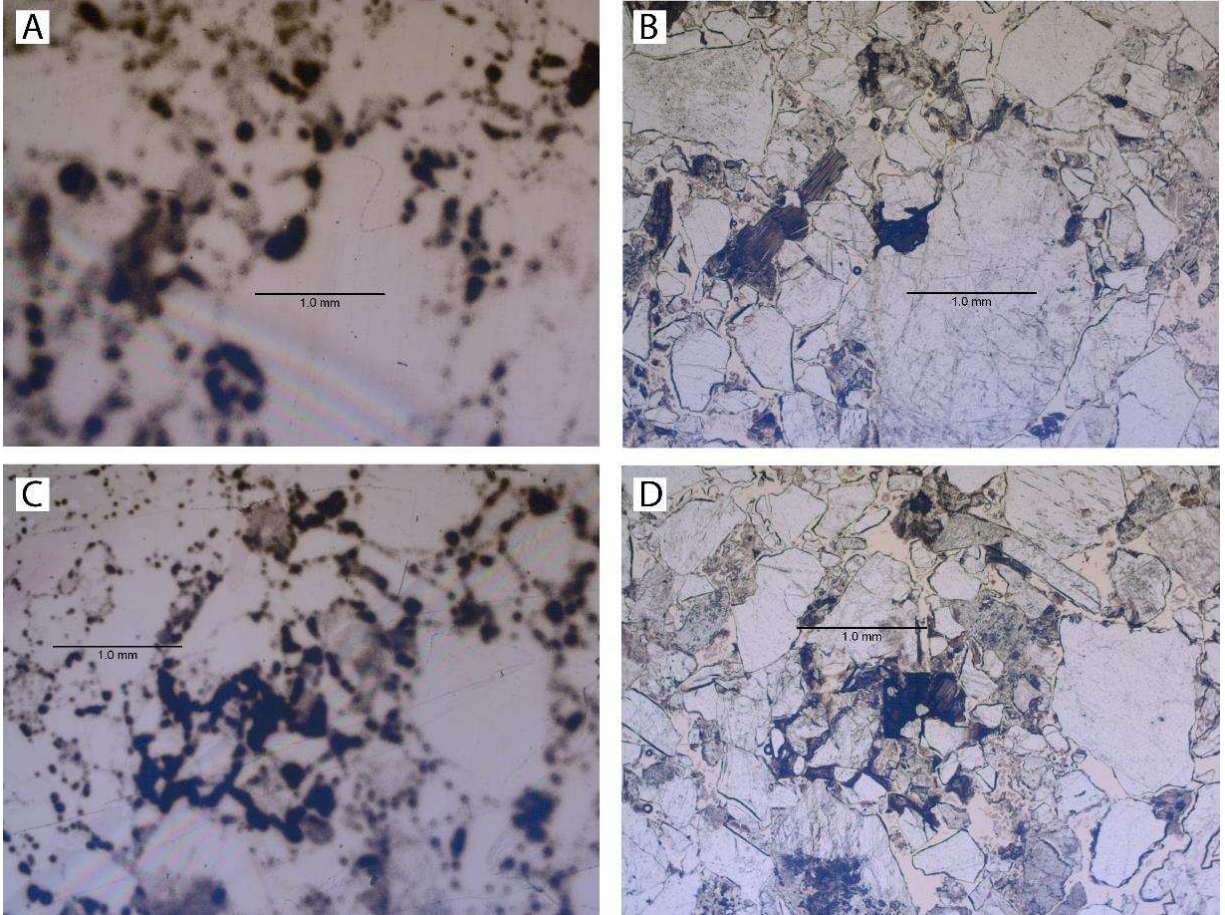
Figure 2.7. A) Fission track map of sample 13C: 412-413, showing the distribution of uranium bearing minerals. B) Transmitted light image of the same area shown in (A). C) Fission track map of sample 13C: 412-413, showing uranium concentrated in the matrix. In the top left of the photo, scattered point sources occurring between grains with little to no matrix. D) Transmitted light image of the same area shown in (C).

Uranium can occur as speckled hot spots (Figs. 2.8 A-B) or be more homogeneously distributed throughout a clay matrix (Fig. 2.8 C-D). Uranium concentration is highest near grain surfaces, occurring as grain coatings (3.0-12.0 wt. % U) compared to U in the matrix. In some instances, grain coatings can contain over 17 wt. % U and be present between larger framework grains with no matrix present (Fig. 2.9A-B). Moderate uranium concentration (4.0-9.0 wt. % U) were rarely found in a clay matrix, however Figure 2.9C-D is one such occurrence. From the mapped areas, the uranium grain coatings show no preference as to which framework grains (quartz, plagioclase, or orthoclase) to adhere. The highest-grade uranium minerals contain as much as 26.0 wt. % U. Two of these high-grade minerals occur within ~200 microns of one another (Fig. 2.9E-F) while the final occurrence appears in a matrix of moderate grade (~6 wt. % U) (Fig. 2.9D).

2.4.4   Automated Mineralogy

Automated mineralogy analyses were performed on a total of four samples, two from each the Lost Creek Project and the TCEA.

2.4.4.1 Lost Creek

Using the bright phase search setting using an SEM-based automated mineralogy system, a total of 5 areas containing uranium bearing minerals were found in sample 13C: 412-413 from the Lost Creek Project; in sample 11C: 446-447 from the Lost Creek Project, no uranium minerals were identified. All 5 U findings are associated with clay minerals surrounding framboidal pyrite. In mineral modal analysis mode in automated mineralogy, the clay mineral was identified as illite and kaolinite. Figure 2.10 represents a high-resolution scan of one of the U findings and displays a small core of uraninite within a larger mass of an unknown Ca- and Si-bearing U mineral near a mass of framboidal pyrite. A similar uranium mineral can be seen in Figure 2.11. This unknown Ca- and Si-bearing U mineral is usually concentrated around framboidal pyrite and occurs as grain coatings along quartz grains which are cemented by calcite.
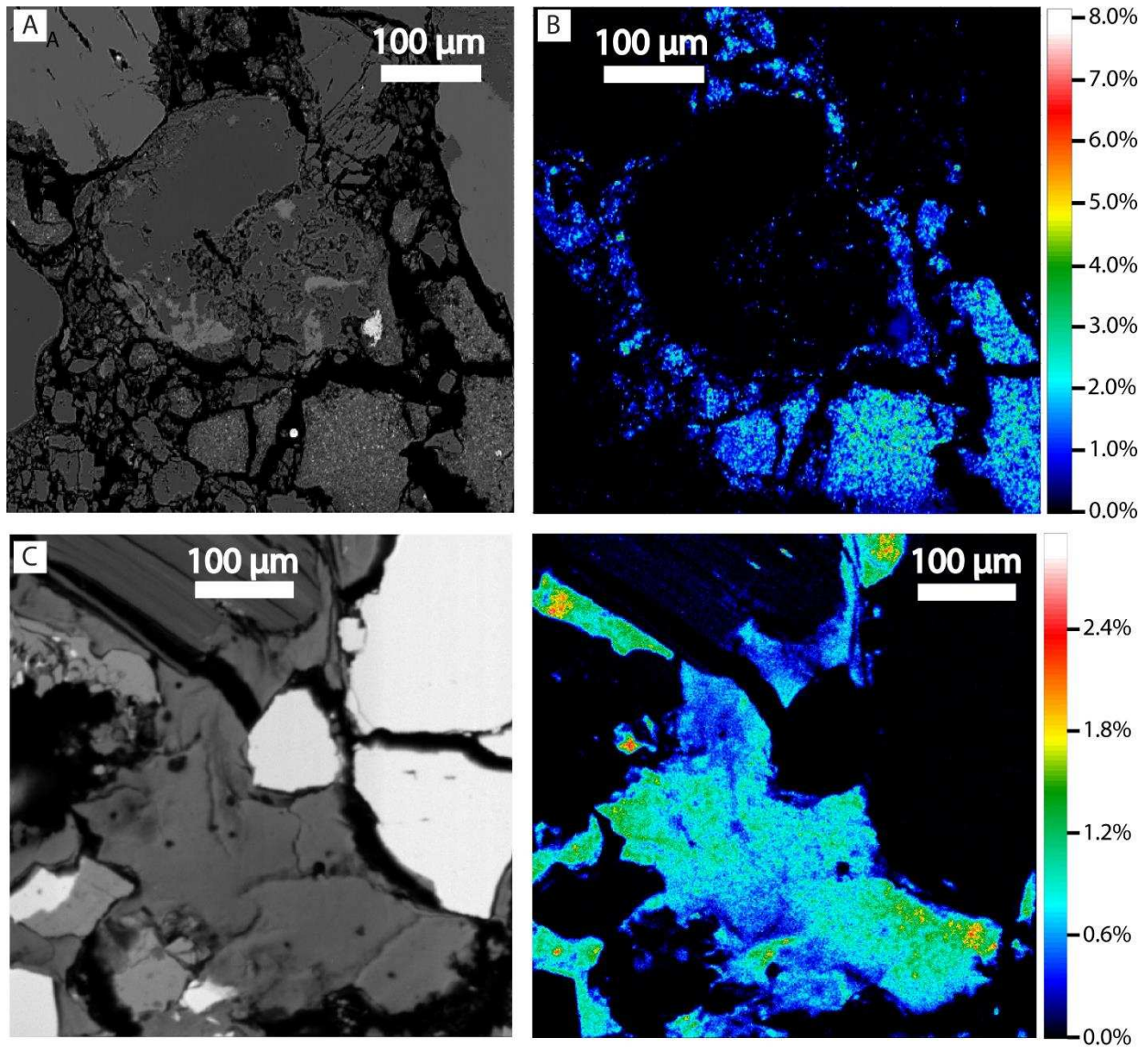
Figure 2.8 A) BSE image of sample 11C: 446-447 from Lost Creek with uranium disseminated in clay matrix and the corresponding false-colored uranium distribution map (B). B) Moderate concentrations of uranium are disseminated throughout clay minerals. C) Si distribution map of sample 13C: 412-413 from Lost Creek and the corresponding false-colored uranium distribution map (D). Uranium disseminated in clay minerals has a range of concentrations including low-grade areas with less than 1 wt. % U.
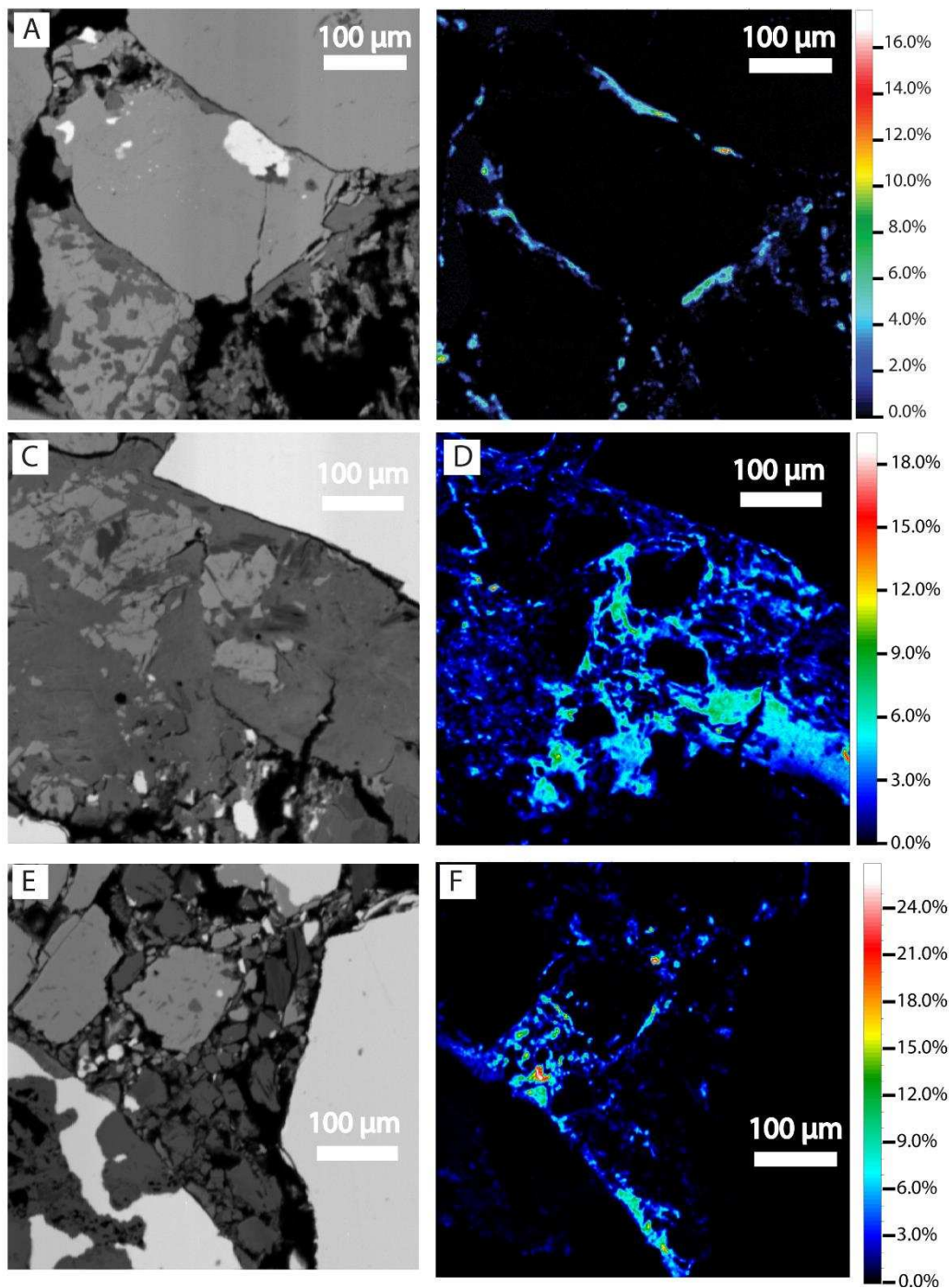
Figure 2.9 A) Si distribution map of sample 11C: 446-447 with the brightest areas representing the highest concentrations of Si B) Uranium distribution map detailing the grain coating features of the uranium mineral C) Si distribution map of sample 13C: 412-413 with moderate uranium concentrations within the matrix and the corresponding uranium distribution map (D) Uranium is disseminated throughout clay minerals and are often highly concentrated around framboidal pyrite (bottom right). E) Si distribution map of sample 11C:446-447 from the Lost Creek Project showing   high-grade uranium area (F) Uranium concentration map highlighting uranium occurring as grain coatings and two discrete high grade uranium minerals.
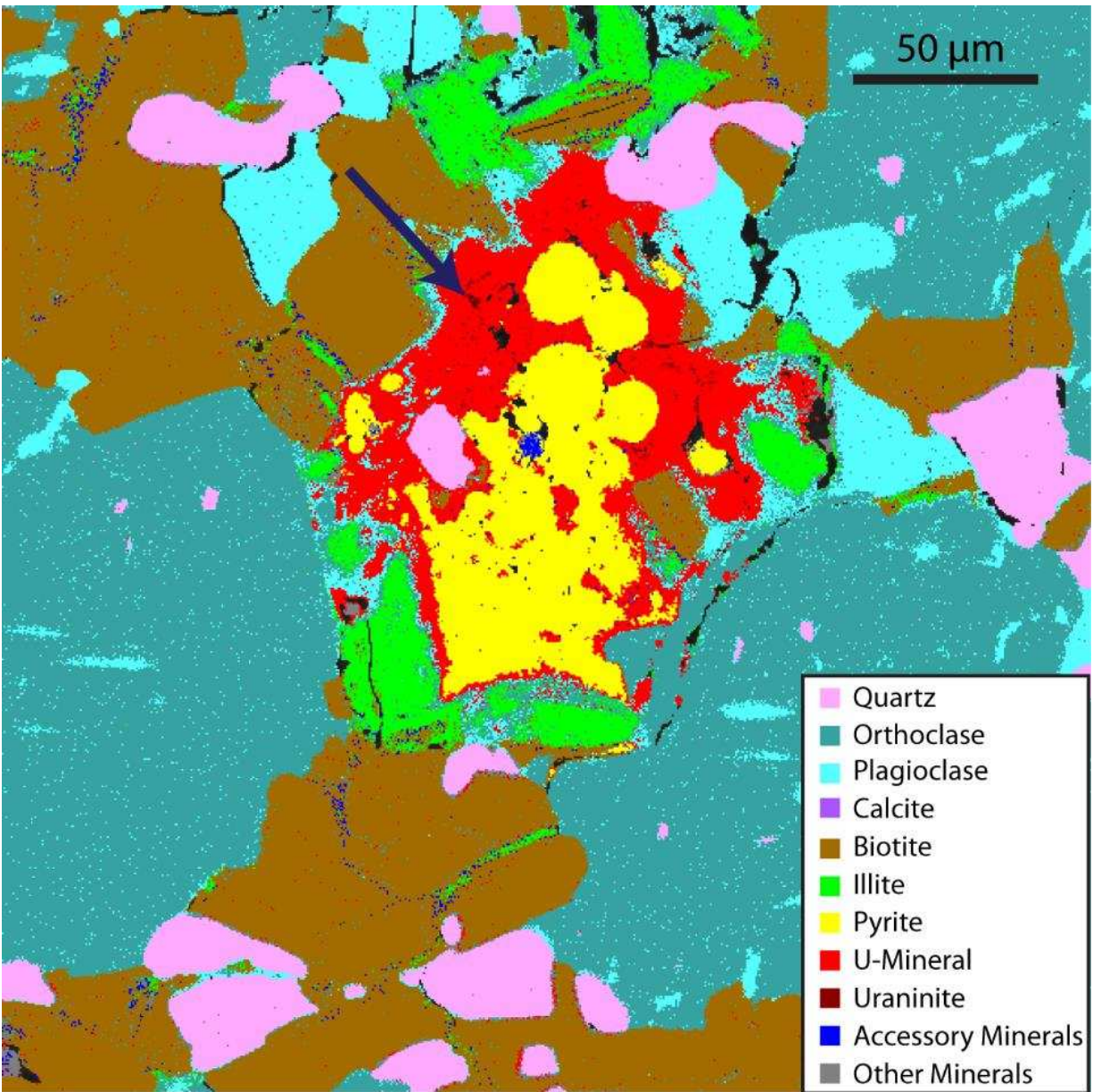
Figure 2.10. False-colored automated mineralogy image of a high-grade uranium mineral surrounding framboidal pyrite from sample 13C: 412-413. A small core of uraninite was identified (arrow).

2.4.4.2 Three Crow

Two samples from the TCEA were analyzed using the bright phase search feature in automated mineralogy. In sample H-161C-W, a uranium mineral was found coating the surface of multiple diagenetic pyrite grains (Fig. 2.12). EDS analysis results indicate that the mineral is

composed of U, P, V Si, Al and O. No uranium mineralization was identified in sample H-161C-002F.
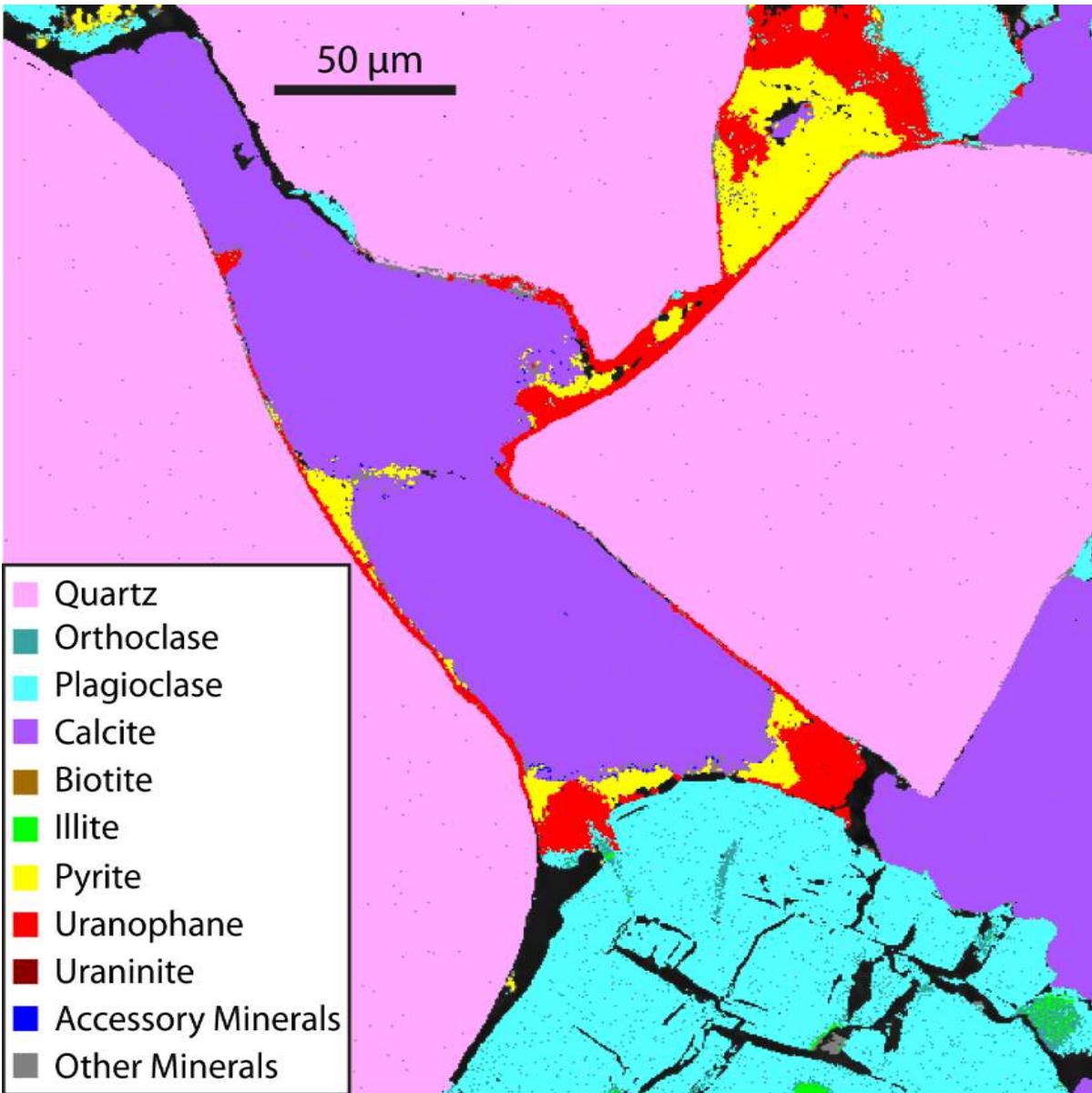
Figure 2.11 False-colored automated mineralogy image of Ca- and Si- bearing U mineral associated with pyrite framboids and as grain coatings on quartz grains from sample 13C: 412-413.
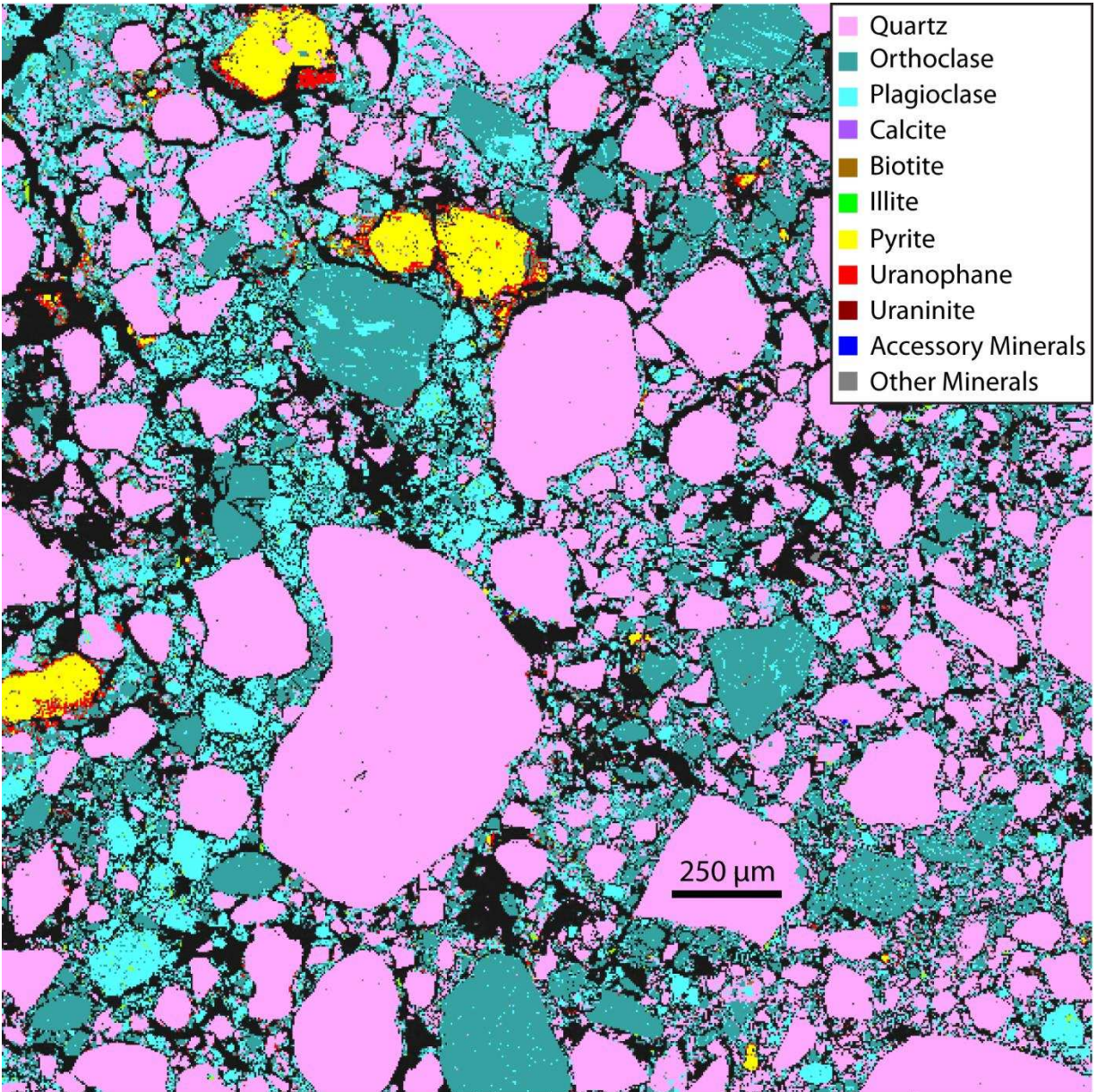
Figure 2.12 False-colored automated mineralogy image of sample H-161C-W from the TCEA. Uranium minerals adhere to large pyrite grains coating the surface.

2.4.5 Field emission scanning electron microscopy

Using the SEM equipped with a field emitter electron source, BSE images and EDS point analyses of areas with elevated U concentrations were collected for samples 13C: 412-413 and 11C: 446-447 from the Lost Creek Project and samples H-161C-W and H-161C-002F from the TCEA.
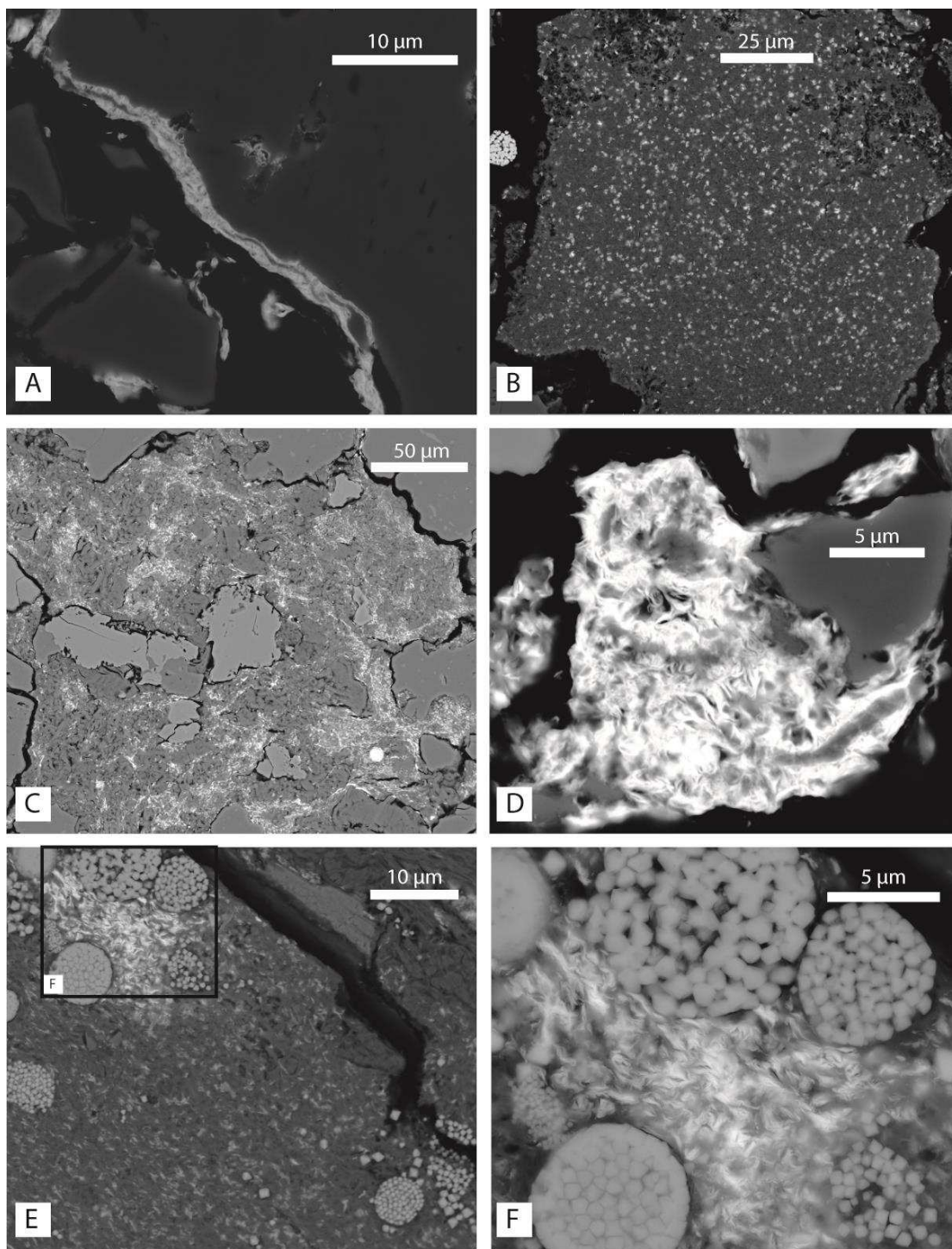
Figure 2.13 BSE images of uranium bearing minerals from samples 11C: 446-447 and 13C: 412-413. A) Uranium mineral coats the outside of an albite grain. B) Uranium mineral spread throughout a clay mineral. C) Uranium mineral distributed throughout clay minerals. D) A high-grade uranium mineral intertwined with clay. E) Uranium mineral disseminated throughout clay with a local enrichment near pyrite framboid. F) Closeup of high-grade area in E.
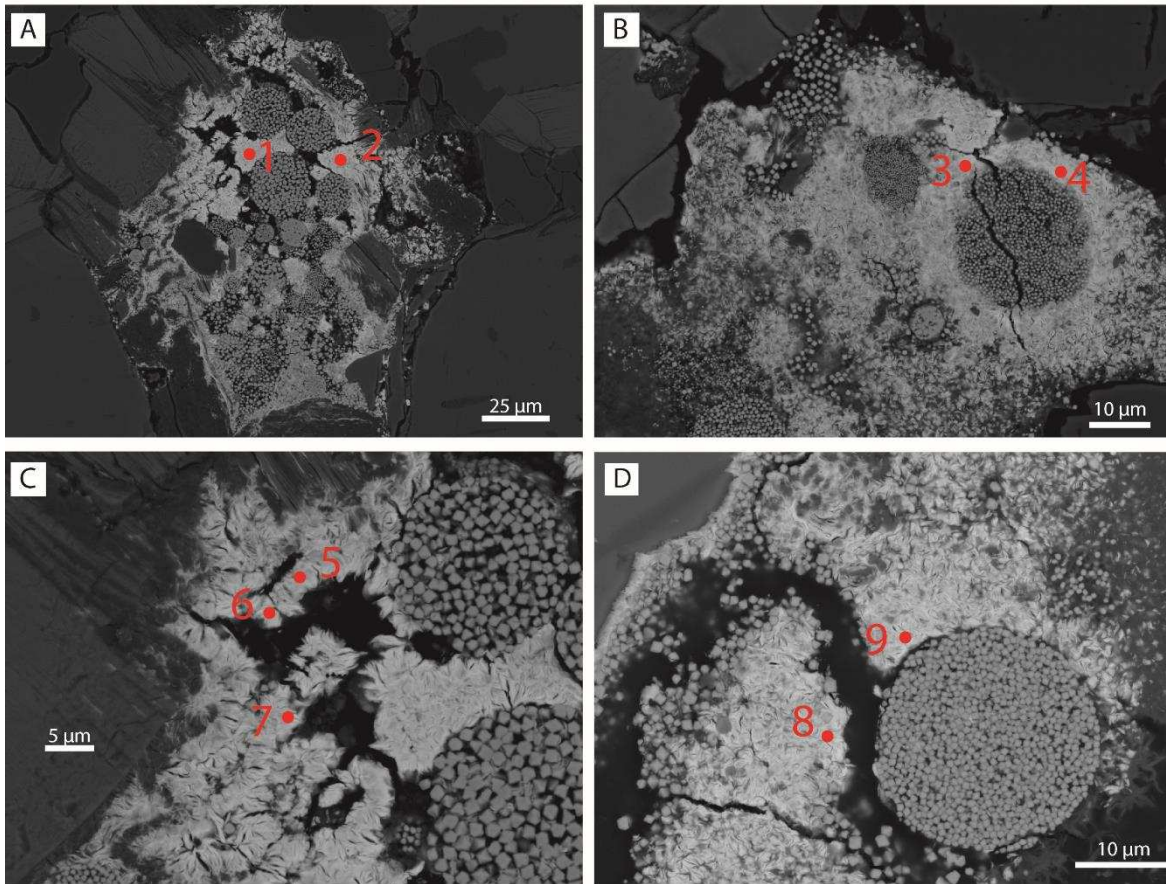
Figure 2.14. BSE images of uranium bearing minerals from sample 13C: 412-413 with EDS point analyses locations. Results in Table 1. A) Area of concentrated uranium intergrown with framboidal pyrite. B) Disseminations of uranium bearing minerals intergrown with pyrite and clay. C) Closeup image of uranium bearing mineral adsorbed onto the surface of altered feldspar. D) Dense concentrations of uranium bearing mineral with increasing uranium concentrations closer to the pyrite framboid.

2.4.5.1 Lost Creek

In Fig. 2.13A, the wispy uranium mineral can be seen coating a large albite grain and is relatively uniform in thickness measuring 2-3 µm. In Figure 2.13B, the uranium mineral is disseminated throughout a clay matrix occurring as 1-2 µm wisps creating a speckled pattern. The uranium mineral occurs randomly within the clay matrix and is homogeneously distributed throughout. In Fig. 2.13C, the uranium mineral displays an affiliation with illite while being absent in kaolinite creating a patchy matrix with respect to uranium content. The high-grade mineral identified with the microprobe (Fig. 2.8F) is a dense, irregular accumulation of wisps of

uranium bearing mineral coating smaller grains of albite and disseminated in illite (Fig. 2.13D). In all areas imaged, only one variety of uranium bearing mineral was detected using the FE-SEM (Fig. 2.13). In samples 13C: 412-413 and 11C: 446-447 the U-bearing mineral occurs as small (~1 µm), wispy or fibrous phases, either as individual wisps or as a bulk accumulation often found coating framework grains (Fig. 2.13). In Fig. 2.13E, the density of the U-bearing mineral varies from low density where the U mineral occurs as ~1 µm wisps throughout illite to an area of high density located in between several pyrite framboids. However, not all framboidal pyrites are associated with an increased uranium concentration. Figure 2.13F, is a close-up of the high density area in Figure 2.13E, where the wispy nature of the uranium mineral is visible occurring as small ~1 µm wisps in illite.

Semi-quantitative EDS analyses were conducted in order to identify uranium bearing minerals. Spot analyses were selected based on brightness and isolation from other phases such as pyrite and clay minerals. In Figure 2.14A, a large population of framboidal pyrites, with diameters up to 25 µm and euhedral pyrite aggregates ranging in size from <1 µm to ~2 µm, are surrounded by a dense concentration of the fibrous U-bearing mineral which occurs as wisps that are 2-3 µm in size. The uranium mineral is found within illite with interstitial euhedral pyrite. Two spot analyses were taken from high-grade areas; Spot 1 has high Ca and U values (13.1 and 20.7 atom %, respectively) with very little Si (1.5 atom %), and no Al, while Spot 2 has 11.2 atom % U, 6.8 atom % Ca, 9.1 atom % Si, and 5.1 atom % Al (Fig. 2.14A; Table 1). In Figure 2.14B, the uranium mineral is found within illite with interstitial euhedral pyrite. The concentration of the uranium mineral decreases with distance from the ~20 µm framboid and with decreasing pyrite content. Two spot analyses were taken proximal to the large framboid. Spot 3 contains 13.1 atom % U, 8.4 atom % Ca, 3.1 atom % Si and 0.5 atom % Al and Spot 4 contained 16.6 atom % U, 9.8 atom % Ca 2.8 atom % Si and 0.4 atom % Al (Fig. 2.14B; Table 1). The uranium mineral is generally constrained to illite, although mineralization does occasionally occur within framboidal pyrites (Fig. 2.14C). The dense accumulation of the U-bearing mineral in Figure 2.14C was chosen for spot analyses of which three were taken. Spot 5 has the lowest U and Ca content at 13.0 and 7.7 atom %, respectively and the highest Si content at 7.4 atom %. Spot 7 has the highest U and Ca concentration of the analyses from Figure 2.14C, at 14.5 and 9.2 atom % with a Si content of 3.7 atom %. Spot 6 has a U concentration of 14.3 atom %, a Ca concentration of 8.5 atom % and the lowest Si content at 1.6 atom % (Table 1).

Table 2.1. Results from EDS analysis from Figure 2.14 in atom %

	O	Al	Si	Ca	Fe	U
Spot 1	64.7	0.0	1.5	13.1	0.0	20.7
Spot 2	65.3	5.1	9.1	6.8	2.5	11.2
Spot 3	74.9	0.5	3.1	8.4	0.0	13.1
Spot 4	70.3	0.4	2.8	9.8	0.0	16.6
Spot 5	70.1	1.8	7.4	7.7	0.0	13.0
Spot 6	75.6	0.0	1.6	8.5	0.0	14.3
Spot 7	70.6	0.0	3.7	9.2	2.1	14.5
Spot 8	73.2	0.5	3.8	8.7	0.0	13.7
Spot 9	70.5	2.9	8.3	7.1	0.0	11.2

In Figure 2.14D, uranium mineralization occurs as grain coatings (1-2 µm thick). Spot 8 has a U content of 13.7 atom % with 8.7 atom % Ca and 3.8 atom % Si. Spot 9 has less U and more Si at 11.2 atom % and 8.3 atom % respectively with 2.9 atom % Al and 7.1 atom % Ca (Table 1).

2.4.5.1 Three Crow

For FESEM analysis, sample H-161C-W was used due to abundant uranium-bearing minerals identified using automated mineralogy. Spots identified with automated mineralogy were the primary targets of this analysis. At least three different morphologies were identified and are all concentrated proximal to pyrite. The first, and most common uranium mineral, is a euhedral, pellet shaped mineral measuring 3 µm in length and 0.5 µm in width (Fig. 2.15A). The mineral is most commonly found disseminated throughout a vanadiferous clay and is concentrated near iron sulfides. The second morphology is a massive, irregularly shaped mineral that appears less bright (lower atomic Z) than the euhedral, pellet shaped mineral. In Figure 2.15B, the massive mineral can be found completely surrounding the pellet shaped uranium mineral. This mineral can also be found intermixed with clay minerals. The third variety is the least common of the identified uranium minerals and was only identified in one location. The mineral is crumbly and irregular, occurring in masses that are approximately 5 µm in diameter. The highest-grade areas are within vanadiferous clays near iron sulfides (Fig. 2.15D). The massive mineral (Spot 2) contains the most U, V, and P at 15.1 %, 3.8 %, and 7.1% respectively (Table 2.2). It also has the lowest Si and Al content at 1.5% and 0.9% respectively. The crumbly mineral contains 12.3 % U, 0.9 % P, and 11.1 % Si (Table 2.2). The lowest concentration of U is

found in the euhedral, pellet mineral (Spots 3 & 4), which contains 9.7 % U, 2.3 % P, 2.3% Ca, and 10.1 % Si (Table 2.2).
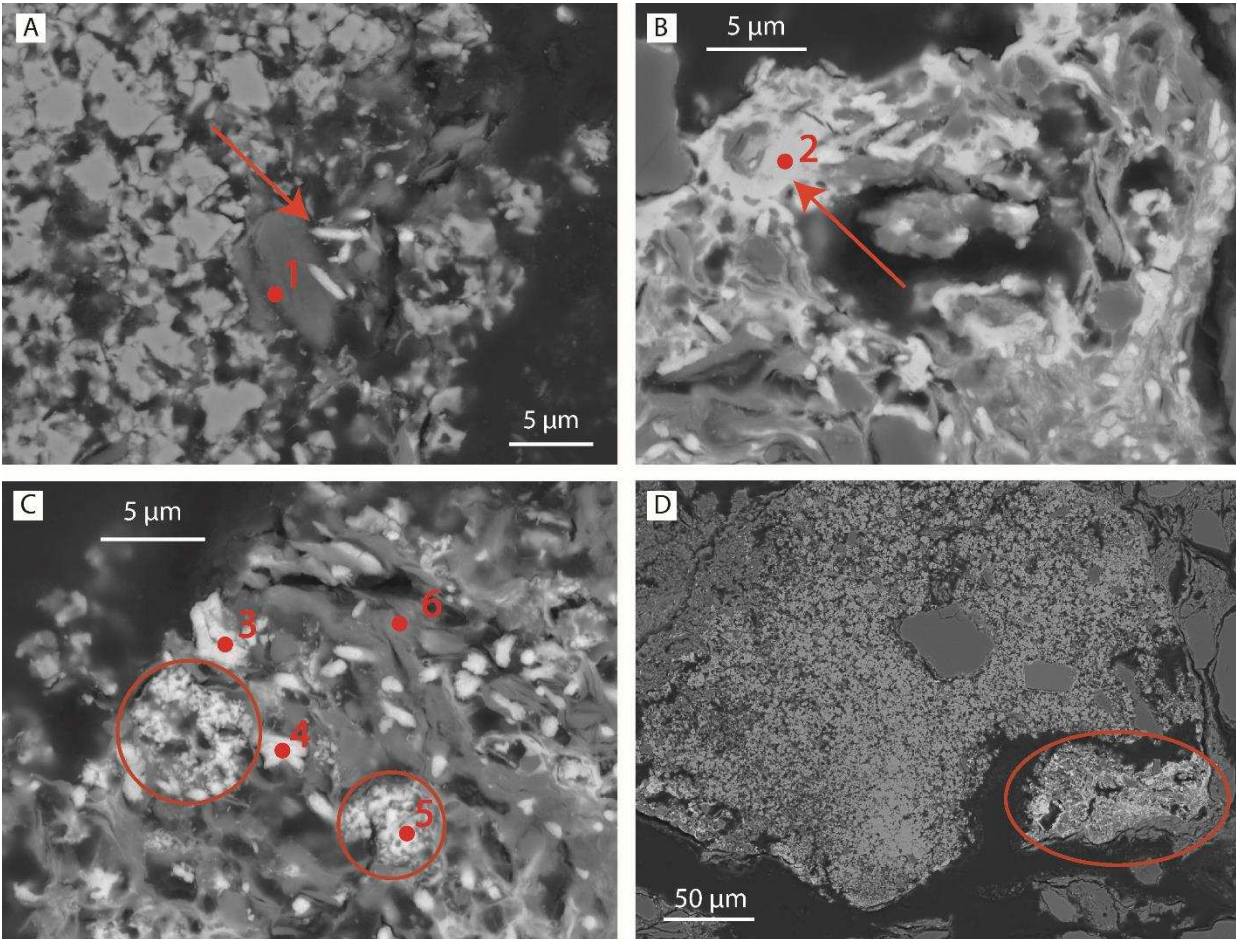
Figure 2.15. FESEM images of sample H-161C-W. A) Pellet-shaped uranium mineral within vanadiferous clay. B) Massive, irregular uranium mineral. C) Crumbly, irregular uranium minerals. D) High-grade uranium area hosted in a vanadiferous clay.

Table 2.2. Results from EDS analysis from Figure 2.15 in atom %.

	O	Na	Mg	Al	Si	P	S	K	Ca	V	Fe	U
Spot 1	62.6	-	-	14.1	16.8	-	3.3	-	-	0.6	2.2	0.4
Spot 2	60.1	-	-	0.9	1.5	7.1	4.1	-	-	3.8	7.4	15.1
Spot 3	68.0	1.1	-	1.2	10.1	2.3	0.7	-	2.3	1.8	2.8	9.7
Spot 4	66.9	-	-	1.6	14.3	2.0	0.6	-	2.1	1.8	2.2	8.6
Spot 5	67.7	1.3	-	0.8	11.1	0.9	0.7	3.3	-	-	1.9	12.3
Spot 6	59.8	1.0	1.3	9.7	22.8	-	-	-	-	2.1	1.8	1.6

2.4.6 Transmitted electron microscopy

A FIB cutout of the high grade mineral from Lost Creek Project sample 11C: 446-447, displayed in Figure 2.16, was the target of multiple TEM analyses. TEM analyses were conducted to highlight the nature of the uranium mineral including elemental composition, crystal habit, and additional mineral characteristics at a higher resolution. In Figure 2.16A, the HAADF image shows the laminar structure of the uranium bearing mineral is consistent at higher resolutions, occurring as grain coatings. Elemental maps were produced to distinguish the relationship between the elements of interest which were identified from FE-SEM EDS analysis of the uranium bearing mineral and include U, Ca, Al, and Si (Fig. 2.16B-F). Using the elemental maps, it is evident that the uranium concentrations are positively correlated with calcium and negatively correlated with aluminum, silicon, and sodium.

A total of 3 line scans were taken at multiple locations across the cutout from sample 11C: 446-447. In Fig. 2.17, the line scan was positioned to intersect predominantly high grade uranium and also some of the interfingered clay minerals. Another line scan was performed to intersect some of the larger aluminosilicate grains and the uranium bearing, grain coating mineral (Fig. 2.18). The line scans indicate a positive correlation between the uranium (up to 39.0 atom % U) and calcium (up to 15.8 atom % Ca) contents. The negative correlation between the Al and Si content and the U is also evident with the highest U concentrations concordant with the lowest Al and Si contents. The line scan results give an elemental composition (in atom %) of approximately 27- 35%, Si from 35-45%, and the Al and Ca content both between 11- 17%.

Using the elemental maps it is evident that the uranium is positively correlated with calcium content and negatively correlated with aluminum, silicon, and sodium. Line scans taken at multiple locations (Fig. 2.17-2.18) consistently measure the U content of the mineral at approximately 30-35 atom %, the Si from 35-45 atom % and the Al and Ca both between 10-15 atom %. From spot analyses (Fig. 2.19), the U-bearing phases contain $10 - 14$ atom % U and between 1-3 atom % Ca. Within the uranium bearing mineral silicon composition ranges from 71 $- 79$ atom % and aluminum content ranges from $7 - 12$ atom % (Table 2).
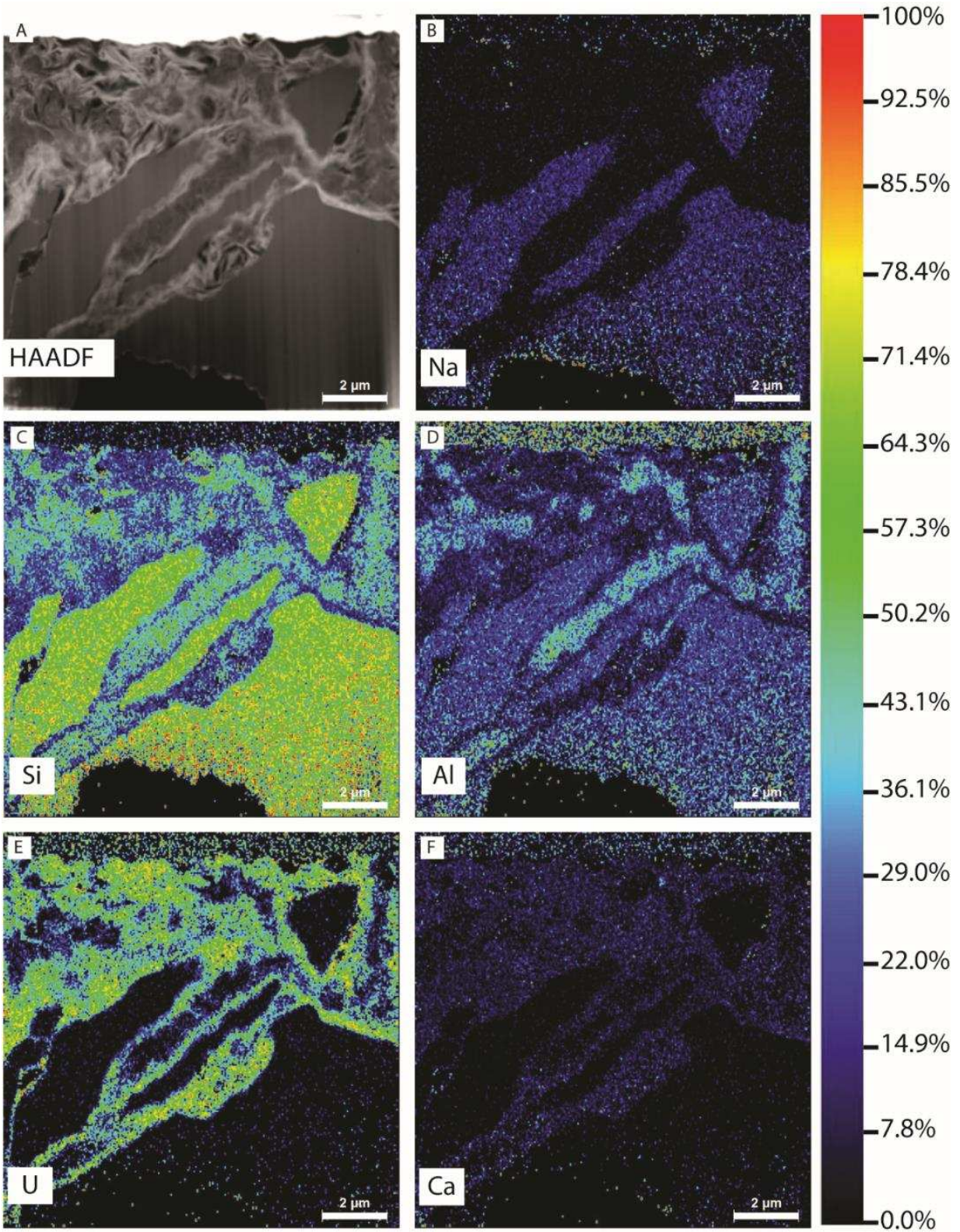
Figure 2.16 A) High-angle annular dark field (HAADF) image and elemental maps showing sodium (B), silicon (C), aluminum (D), uranium (E), and calcium (F) in weight %.
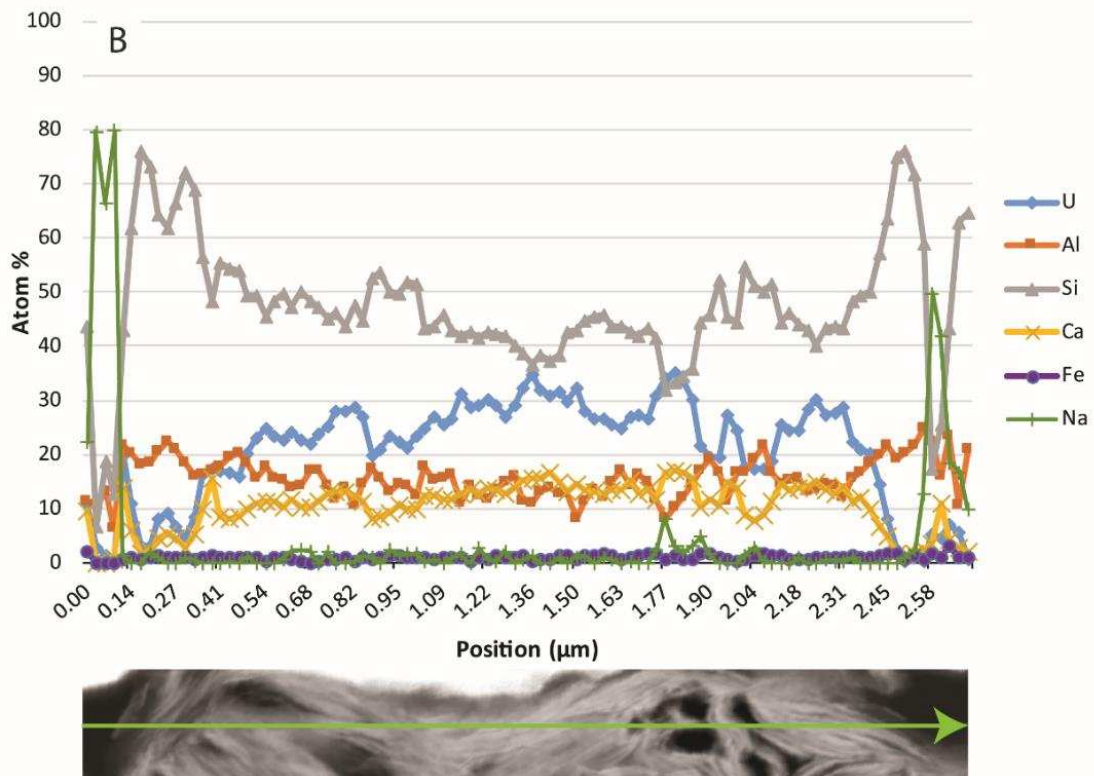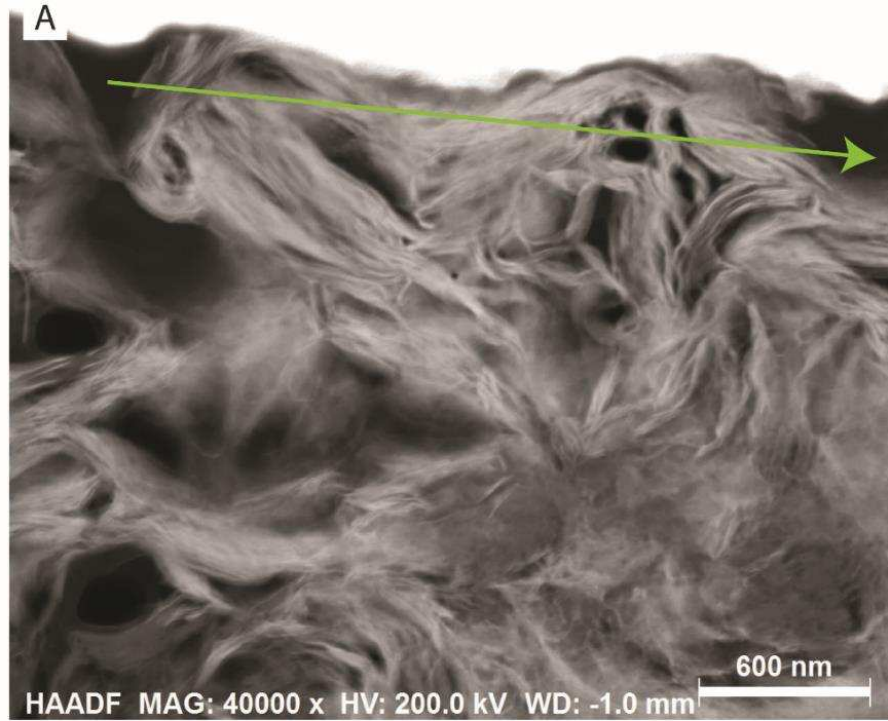
Figure 2.17 A) TEM image of a high-grade uranium area from sample 11C: 446-447 with arrow indicating line scan. B) Results of line scan in atom %.
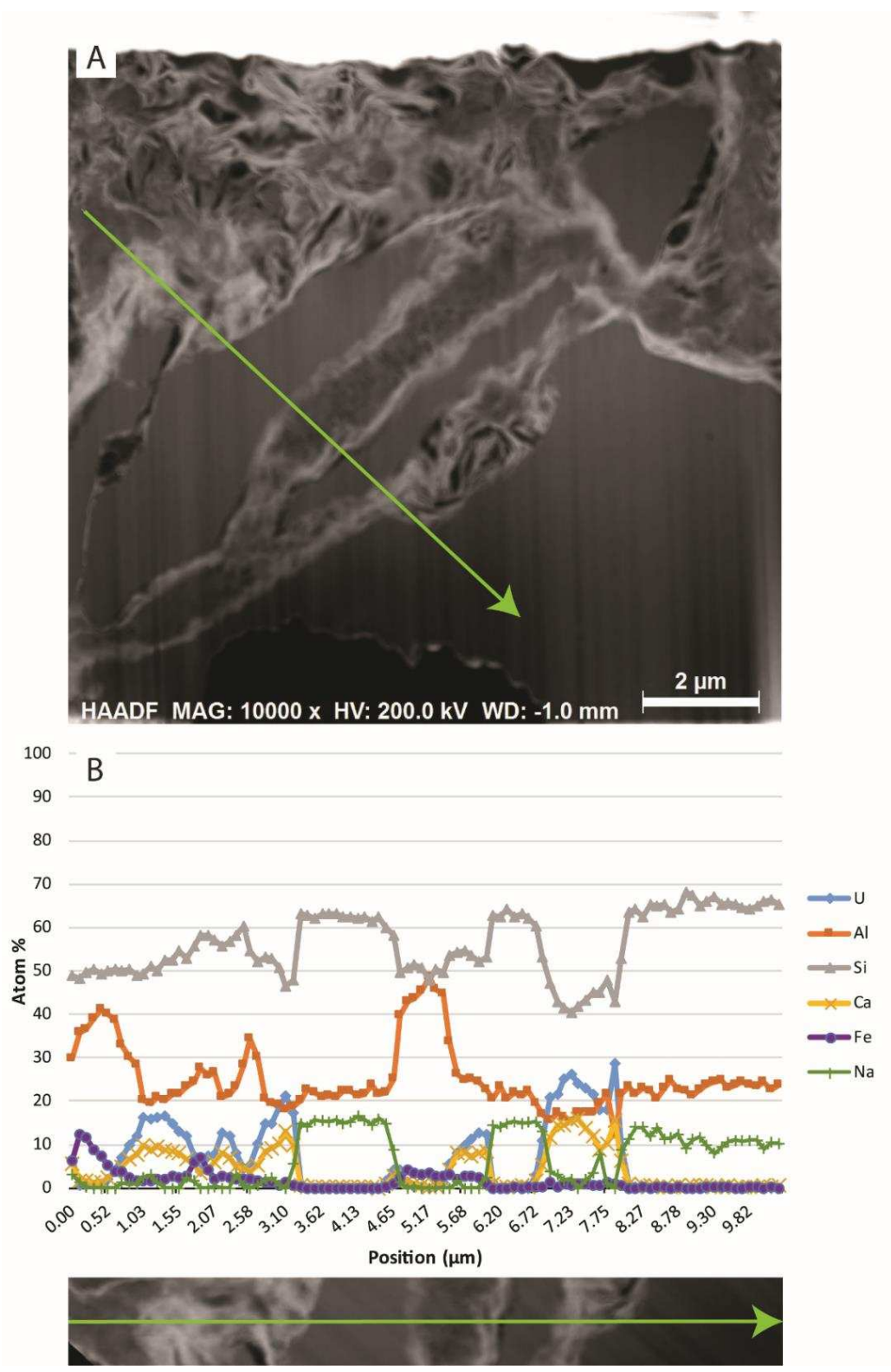
Figure 2.18 A) TEM image of high-grade uranium area from sample 11C: 446-447 with arrow indicating line scan. B) Results of line scan in atom %.
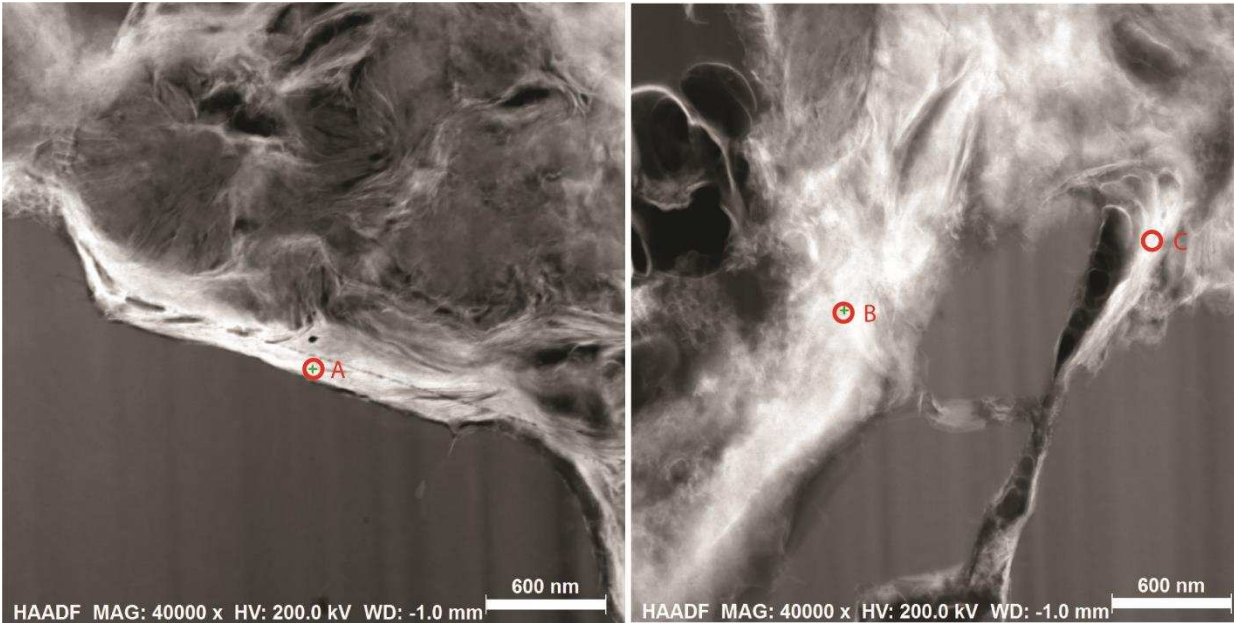
Figure 2.19 HAADF images of the locations chosen for spot analyses from sample 11C: 446-447.

Table 2.3. Results of TEM point analyses (in atom %)

	U	Si	Al	Ca	Fe
Spot A	14	75	7	3	1
Spot B	13	71	13	2	1
Spot C	10	79	9	1	0

2.5   Discussion

In the following section, the results are discussed and evidence is provided to support the identification of the ore mineral at both the Lost Creek Project and the Three Crow Expansion Area and address the factors contributing to the discrepancy between the estimated head grades and initial head grades.

The principal ore minerals in roll front uranium deposits have been described as uraninite and coffinite (Dahlkamp, 1978; Harshman, 1972; Stewart et al., 2000) and less often as the secondary minerals tyuyamunite, $Ca(UO_2)_2(VO_4)_2 \cdot 5\text{-}8H_2O$, carnotite, $K_2(UO_2)_2(VO_4)_2 \cdot 3H_2O$ and autunite, $Ca(UO_2)_2(PO_4)_2 \cdot 10\text{-}12H_2O$ (Adler & Sharp, 1967; Stewart et al., 2000). The formation of secondary minerals is largely dependent on the presence of key metals, particularly P, V, Cu, and Ca (Finch & Davis, 1985).

38

2.5.1 Ore Mineralogy at Lost Creek

Results from the FE-SEM EDS analyses are variable and can be attributed to the fine-grained nature of the uranium phase disseminated throughout a clay matrix. At the Lost Creek Project, uranium mineralization is hosted in an illite and kaolinite clay that has a Si:Al ratio of 2:1 and contains 1.5-1.8 atom % Mg and 1.1-1.6 atom % Fe. Uranium and calcium are positively correlated with a U:Ca ratio ranging from 1.6-1.7 (Table 1). Calcium is only found within the uranium-bearing mineral and is absent from the surrounding clays. A weak positive correlation exists between Si and Al with a Si:Al ratio ranging from 1.7- 7.6, with Al absent altogether in some analyses (Table 1). In analyses with elevated concentrations of Si and Al, such as Spots 2 and 9, the Si:Al ratio is close to 2 (Table 1) and U and Ca contents are lower. This is a result of mixed analyses that include a significant amount of illite/kaolinite, representing the clay matrix. Results from the TEM point analysis suggest the existence of becquerelite (U:Ca ratio of 6:1) where the U:Ca ratio ranges from 5.09-7.00 (Table 2). The uranium ore minerals found using SEM- and TEM-EDS analyses are a mixture of the calcium uranyl silicate, uranophane, $Ca(H_3O)_2(UO_2)_2(SiO_4)_2 \cdot 3H_2O$ and becquerelite $Ca(UO_2)_6O_4(OH)_6 \cdot 8(H_2O)$, mixed with illite clay minerals. Becquerelite and uranophane are both secondary minerals formed from the oxidation of uraninite and are commonly found together (Shvareva et al., 2011). Results from automated mineralogy analyses (Fig. 2.10) provide evidence for the oxidation of uraninite where a small core of uraninite is surrounded by the secondary uranium mineral uranophane in a matrix of kaolinite and minor illite.

Although the TEM has a much higher resolution than SEM analyses, similar problems arising from the fine-grained nature of the uranium minerals are still present. Moreover, the high Si and Al content is interpreted to be a product of fluorescence caused by the high energy Kα X-rays from excited uranium electrons. Unlike the electron beam used by the FE-SEM, the electron beam from the TEM has sufficient energy (200 keV) to excite the electrons located in the K orbital of a uranium atom. The energy released once a K orbital electron is ejected is 97.143 keV, which is sufficient energy to cause fluorescence in nearby atoms of O, Al, Si, and Ca (Gorman, personal communication). Fluorescence occurs when the high energy Kα X-rays ejected from the uranium atom excite electrons from low atomic Z elements (e.g. Al and Si) resulting in inflated counts.

2.5.2 Ore Mineralogy at the Three Crow Expansion Area

Similar to the Lost Creek Project samples, EDS analyses performed with the SEM on the TCEA sample likely includes contamination from the surrounding clays. Much of the Si and Al content is likely due to mixed analyses between the U mineral and intergrown clay minerals. Pyrite framboids show signs of alteration and replacement by uranium minerals. According to the technical report on the TCEA (Crow Butte Resources, Inc. 2010) the uranium mineralogy is cited to be the same ore mineral as in the neighboring Crow Butte mine, which is predominantly coffinite with lesser amounts of uraninite. The abundant euhedral uranium crystal is believed to be coffinite (Fig. 2.15A). A cluster of the euhedral pellets (Fig. 2.15C) were analyzed for composition using SEM-EDS resulting in a U:Si ratio of 1, concordant with the coffinite formula $(U(SiO_4)_{1-x}(OH)_{4x})$. The euhedral pellets also contained 2.1-2.3 atom % Ca and 2.0-2.3 atom % P which are common minor elements in coffinite (Janeczek & Ewing, 1992). The other two phases are more difficult to identify. The massive, irregular mineral (Fig. 2.15B) may be the uranium phosphate, ningyoite, $(U, Ca, Ce)_2(PO_4)_2 \cdot 1\text{-}2H_2O$, although it contains a significant amount of vanadium. According to the TCEA report (Crow Butte Resources Inc., 2010), tyuyamunite, a calcium bearing uranyl vanadate, is present within the deposit, however, this could not be verified. The uranium mineralogy at the TCEA appears to be dominated by coffinite, although other uranium bearing phases, possibly ningyoite, are also present.

2.5.3 Differences in Ore Mineralogy at the Lost Creek Project and TCEA

Uranophane and becquerelite are common secondary minerals often found on the surface of altered uraninite (Wronkiewicz et al., 1992). Multiple studies on the alteration of uraninite to form secondary minerals have been conducted (Finch & Ewing, 1992; Shvareva et al., 2011; Wronkiewicz et al., 1992; Perez, 2000). Under oxidizing conditions, the surface of uraninite is host to uranyl silicates (Finch & Ewing, 1992). However, the direct precipitation of uranyl silicates requires a high concentration of Si in solution (Shvareva et al., 2011; Figs. 2.20 and 2.21). With low to moderate Si in solution, the mixed precipitation of two uranyl hydroxides occurs: schoepite $(UO_2)_8O_2(OH)_{12}(H_2O)_{12}$ and metaschoepite $UO_3(H_2O)_2$. The precipitation of these minerals is then followed by the dehydration and structural rearrangement forming dehydrated schoepite, calculated at approximately $UO_3 \cdot 0.8H_2O$ (Finch & Ewing, 1992). If sufficient Ca^{2+} is available in solution, the replacement of schoepite by becquerelite,

$Ca(UO_2)_6O_4(OH)_6 \cdot 8(H_2O)$, is likely, especially at higher pHs. Exposure of schoepite and becquerelite to groundwaters under oxidizing conditions with abundant Ca^{2+} and Si can lead to the minerals' alteration into uranyl silicates, predominantly soddyite, $(UO_2)_2(SiO_4) \cdot 5H2O$ and uranophane, $Ca(H_3O)_2(UO_2)_2(SiO_4)_2 \cdot 3H_2O$. Finch and Ewing (1992) also report that becquerelite, $Ca(UO_2)_6O_4(OH)_6 \cdot 8(H_2O)$, is stable at high silica contents evidenced by contact with muscovite and often coexists with uranophane (Shvareva et al., 2011). Figure 2.21 shows the stability fields of uraninite and uranophane at Ca^{2+} activities of 10^0, 10^{-2}, and 10^{-4} moles and in Figure 2.22, the stability fields of uraninite and uranophane are also shown at $SiO_{2(aq)}$ activities of 10^0, 10^{-2}, and 10^{-4} moles. Favorable conditions for forming uranophane and becquerelite are under oxidizing conditions, at higher pHs with higher $SiO_{2(aq)}$ and Ca^{2+} activities (Figs. 2.21 and 2.22; Shvareva et al., 2011).

Differences in ore mineralogy between the Lost Creek Project and the Three Crow Expansion Area arises from the differences in host rock composition. The ore zones analyzed from Three Crow contain up to 1.76 wt. % organic carbon (Liebold, 2013). In contrast, no
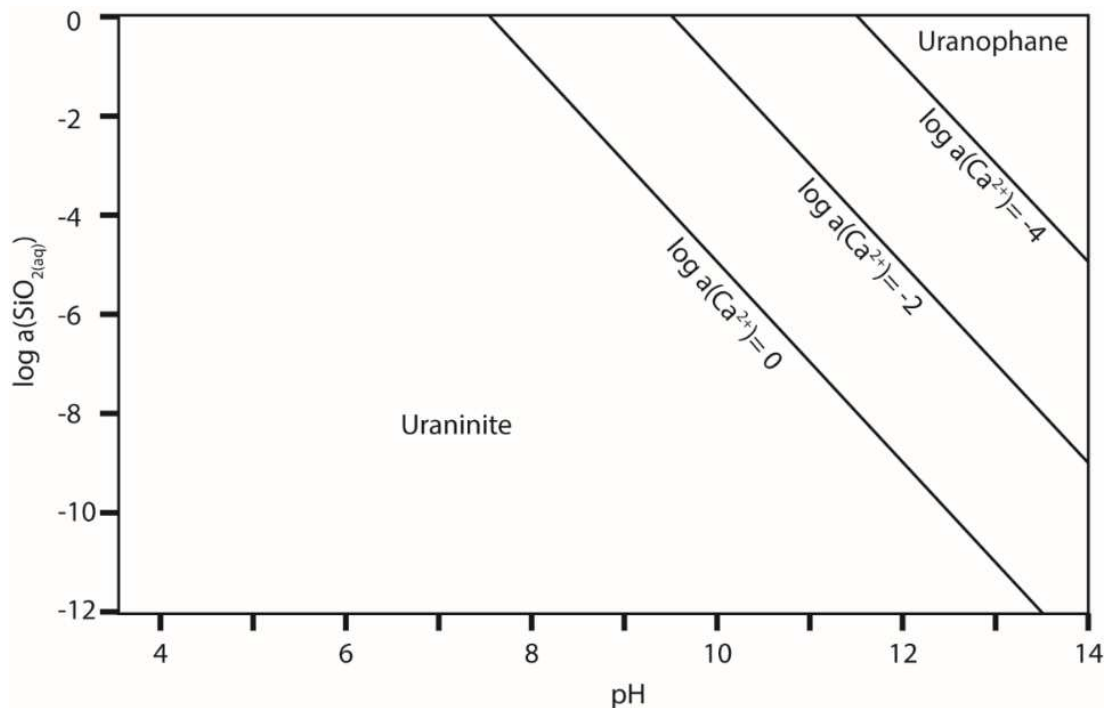

Figure 2.20. The uraninite/uranophane equilibrium as a function of pH and SiO_2 activity at different Ca^{2+} activities. All thermodynamic data can be found in Table 4.

organic matter was found in samples from the Lost Creek Project and the uranium mineralogy at the Lost Creek Project includes the uranyl minerals uranophane and becquerelite which are indicative of a more oxidized environment.
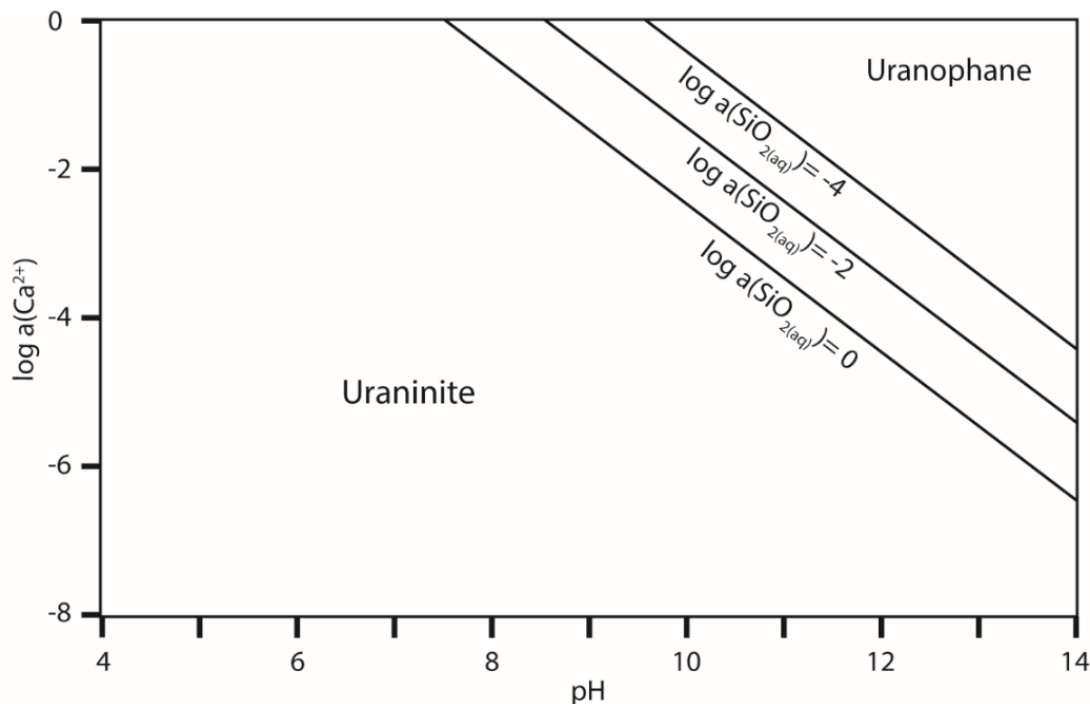
Figure 2.21. The uraninite/uranophane equilibrium at different SiO (aq) activities as a function of pH. All thermodynamic data can be bound in Table 4.

2.5.4 Uranophane and Becquerelite Solubility

As the operators at Lost Creek Project did not know the ore mineral, leaching tests were performed to identify the composition of the most efficient leaching solution. The lixiviant employed contains 2.4×10^{-2} mol/L of $NaHCO_3$ and 1.5×10^{-2} mol/L of H_2O_2 which obtained a U recovery rate of 93.0% with a concentration of 3.9×10^{-4} mol/L of U after a leach period of 16 hours (Ur-Energy Inc., 2016). Initial head grades in the 4th quarter of 2013 contained 211 ppm U, over 5 times the pre-operational estimates with head grades still at 42 ppm in the 4th quarter of 2016. In this study, becquerelite was identified to be one of the main U minerals present at Lost Creek. Solubility studies performed by Gorman-Lewis et al. (2008) at varying pH, solubility is with 250 ppm highest at a pH between 7 and 9, with $CaUO_2(CO_3)_3^{2-}$ being the dominant aqueous

Table 2.4. Thermodynamic input data and respective references

Species	$\Delta G^\circ_{f,298}$ (kJ/mol)	$\Delta S^\circ_{f,298}$ (J/mol*K)	Molar volume (cm^3)	Citation
Uranophane	-6800	-2014.6	215.33	Shvareva et al., 2011
Uraninite	-1031.7	77.03	24.618	Robie & Hemingway, 1995
Ca^{2+}	-552.79	276.14	-	Shock et al. 1997
$SiO_2(aq)$	-199.19	9.95	-	Shock & Helgeson, 1988
$UO_2(CO_3)_3^{4-}$	-2660.91	38.446	-	Guillaumont et al., 2003

U species. Initial head grades at Lost Creek of 211 ppm are in good agreement with becquerelite being a major contributor to the U mineralogy at Lost Creek.

Solubility studies on uranophane show that uranophane can be dissolved in acidic conditions as well as alkaline conditions. The dissolution of uranophane using a bicarbonate lixiviant is represented in Eq. (2).

$$Ca(H_3O)_2(UO_2)_2(SiO_4)_2 \cdot 3H_2O + 6HCO_3^- \rightarrow Ca2UO_2(CO_3)_3^{2-} + 2H_4SiO_4 + 5H_2O \qquad (3)$$

Uranophane dissolution studies have been conducted in previous work including Nguyen et al. (1992) and Perez et al. (2000) which studied dissolution rates in bicarbonate media. According to Perez et al. (2000), the bicarbonate ion is an important complexing agent for aqueous U^{6+}, allowing the U^{6+} to remain in solution and inhibit the formation of secondary phases. Perez et al. (2000) measured the solubility of uranophane in bicarbonate solutions with HCO_3^- concentrations ranging from $1.0x10^{-3}$ to $2.0x10^{-2}$ mol/L. Uranophane solubility peaked at 75ppm at a bicarbonate concentration of $2.0x10^{-2}$ mol/L, which is in good agreement with bicarbonate concentrations used by Ur Energy and with current head grades of 42 ppm reported by Ur Energy (Ur Energy Inc., 2016).

Only minor uraninite, surrounded by uranophane, was found in the samples studied here, and can be neglected in solubility considerations.

2.5.5 Lost Creek Estimation Error

Resource estimations at the Lost Creek Project were performed using gamma ray logs. Resource estimations were made under the assumption that the ore mineral in the deposit was coffinite and uraninite (Ur-Energy Inc., 2016), whereas in this study, the evidence supports the

ore mineral being uranophane and becquerelite. The number of moles of U in a mineral does not necessarily correlate with the activity. Minerals with higher electron densities (higher Z atoms) relative to their molecular weight will have greater adsorption of gamma rays. For a 1g sample of uraninite, the estimated activity in gamma-ray response (GR_{api}), a unit that considers interference in the mineral caused by Compton scattering and photoelectric effects, is 6,010 GR_{api}. A 1g sample of coffinite produces an estimated 5,176 GR_{api}. The same mass of uranophane produces 3,210 GR_{api}, just over half the activity of uraninite. If the resource estimations were made under the assumption that the ore mineral was uraninite or coffinite instead of uranophane, the resource estimations are deflated with respect to uranium content by a factor of 2.

Even if the lesser activity of uranophane would deflate projected initial head grades, additional factors must be in play to account for the initial head grades that were over 5 times higher than estimated. This study proposes that since uranium does not often occur as primary minerals coffinite or uraninite, the geometry of the orebodies, that is dominantly composed of secondary uranyl minerals, is not well defined and therefore resource estimation has been affected. Secondary minerals may exist without any obvious direct spatial relation to the primary ore minerals, which may extend the boundaries of the known resources (Plášil, 2014). The limits of the orebody boundaries may be underestimated due to the mobile nature of the U^{6+} ion.

CHAPTER 3

SUMMARY

3.1   Conclusions

This study was a methods based approach to identify and describe the uranium minerals present at the Lost Creek Project and the Three Crow Expansion Area. Difficulties in analyzing and describing the uranium ore mineralogy stem from the fine-grained nature and their associations with clay minerals. Fission track mapping was invaluable in finding uranium-bearing minerals that might have otherwise gone unnoticed. The sensitivity of this method allowed us to locate low-grade disseminations of U minerals in the samples studied and allowed us to analyze areas of interest with increasing resolution using further analytical techniques including electron microprobe analysis, automated mineralogy, scanning electron microscopy, and transmitted electron microscopy. The use of automated mineralogy excelled at identifying areas of high grade uranium concentration, often associated with framboidal pyrite.

Early resource estimations at the Lost Creek Project assumed that the ore mineralogy was dominated by coffinite with lesser amounts of uraninite. However, the evidence gathered in this study using automated mineralogy, SEM, and TEM analyses supports an ore mineralogy composed of mostly uranophane and becquerelite with minor amounts of uraninite. Uranophane has a gamma ray response (GR_{api}) of almost half of both uraninite and coffinite which would lead to conservative counts during the gamma ray logging of ore zones resulting in an underestimated resource estimate. This, however, cannot explain the initial head grades that were over 5 times higher than initial projections. We propose that the mobile nature of the U^{6+} ion allowed uranium mineralization of secondary minerals to occur away from the primary ore zone leading to a less well defined, larger ore zone.

3.2   Future Work

Based on the findings of the present study, a few areas of future work are recommended. Additional research may not only help with understanding the formation of the two deposits presented in this thesis, but also for roll-front and sandstone hosted uranium deposits in general.

Additional analysis of samples from both deposits would further strengthen the confidence in uranium mineralogy. Due to the expensive nature of the analyses used in this study in addition to the large amount of paperwork required to transport samples that have been subjected to fission track mapping, only a few thin sections from high grade areas were analyzed. A more comprehensive study of a larger sample set, including thin sections from areas with lower gamma ray counts would be helpful in supporting the findings of this study.

A study analyzing the mineralogy and characteristics of uranium ore throughout the different stages of mining. An analysis conducted prior to the introduction of a lixiviant to characterize the nature and amount of uranium in a given sample. A batch or flow through experiment could be conducted using a lixiviant that reflects the solutions used at mine sites. Periodically throughout the experiment, analyze the effects of the lixiviant on the ore mineralogy.

REFERENCES

Adler, H., & Sharp, B. (1967). Uranium ore rolls- occurrence, genesis and physical and chemical characteristics. *Guidebook to the Geology of Utah*, 53-77.

Berning, J., Cooke, R., Hiemstra, S., & Hoffman, U. (1976). The Roessing uranium deposit, South West Africa. *Society of Economic Geologists*, 351-368.

Chadwick, R. (1985). Overview of Cenozoic volcanism in the west-central United States. *Rocky Mountain Section SEPM*, 359-381.

Crow Butte Resources, Inc. (2010). Application for Amendment for USNRC Source Materials License SUA-1534 Three Crow Expansion Area Crawford, Nebraska. *Nuclear Regulatory Commission Technical Report.*

Cuney, M. (2014). Felsic magmatism and uranium deposits. *Bulletin de la Société Géologique de France*, 75-92.

Cuney, M., & Kyser, K. (2009). Recent and not-so-recent developments in uranium deposits and implications for exploration. *Mineralogical Association of Canada*, 79-95.

Dahl, A. R., & Hagmaier, J. L. (1976). Genesis and characteristics of the southern Powder River Basin uranium deposits, Wyoming. *Geology and Resources of the Powder River Basin*, 243-252.

Dahlkamp, F. (1978). Classification of Uranium Deposits . *Mineralium Deposita*, 83-104.

Deditius, A., Utsunomiya, S., & Ewing, R. (2008). The chemical stability of coffinite, $USiO_4 \cdot nH_2O$; $0 < n < 2$, associated with organic matter: A case study from Grants uranium region, New Mexico, USA. *Chemical Geology*, 33-49.

DeGraw, J. (1971). The pre-Oligocene surface in western Nebraska – its relation to structure and subsequent topographies. *Guidebook to the late Pliocene and early Pleistocene of Nebraska, The University of Nebraska Conservation and Survey Division, Nebraska Geological Survey*, 13-22.

Eugster, H. P., & Hardie, L. A. (1975). Sedimentation in an ancient playa-lake complex: the Wilking Peak Member of the Green River Formation of Wyoming. *Geological Society of America Bulletin*, 319-334.

Eugster, H. P., & Surdam, R. C. (1973). Depositional environment of the Green River Formation of Wyoming: a preliminary report. *Geological Society of America Bulletin*, 1115-1120.

Ferret Exploration Company of Nebraska, Inc. . (1987). Application and supporting environmental report for State of Nebraska Underground Injection Control Program. Lincoln, Nebraska.

Finch, R., & Ewing, R. (1992). The corrosion of uraninite under oxidizing conditions. *Journal of Nuclear Materials*, 133-156.

Finch, W., & Davis, J. (1985). Sandstone-type uranium deposits. *IAEA-TECDOC*, 11-20.

Gjelsteen, T. W., & Collings, S. P. (1988). Relationship Between Groundwater Flow and Uranium Mineralization in the Chadron Formation, Northwest Nebraska. *Wyoming Geological Associations Guidebook, 39th Field Conference*, 271-284.

Gorman-Lewis, D., Burns, P., & Fein, J. (2008). Review of uranyl mineral solubility measurements. *Journal of Chemical Thermodynamics*, 335-352.

Grandstaff, D. (1976). A kinetic study of the dissolution of uraninite. *Economic Geology*, 1493-1506.

Guillaumont, R., Fanghanel, T., Neck, V., Fuger, J., Palmer, D., Grenthe, I., & Rand, M. (2004). Update on the chemical thermodynamics of uranium, neptunium, plutonium, americium and technetium. *Elsevier*.

Harris, R. (1984). Alteration and mineralization associated with sandstone uranium occurrences, Morton Ranch area, Wyoming. *WSGS Report of Investigations, 25*, 29.

Harshman, E. (1972). Geology and uranium deposits, Shirley Basin area, Wyoming. *Geological Survey Professional Paper 745*, 1-82.

Harshman, E., & Adams, S. S. (1980). Geology and recognition criteria for roll-type uranium deposits in continental sandstones. *U.S. Department of Energy*.

Hemingway, B. (1982). Thermodynamic properties of selected uranium compounds and aqueous species at 298.15 K and 1 bar and at higher temperatures; preliminary models for the origin of coffinite deposits. *USGS*.

Hoganson, J., Murphy, E., & Forsman, N. (1998). Lithostratigraphic, paleontology, and biochronology of the Chadron, Brule, and Arikaree Formations in North Dakota. *Geological Society of America Special Paper 325*, 185-196.

IAEA. (2016). In situ leach uranium mining: an overview of operations. *International Atomic Energy Agency*.

Liebold, J. (2013). Geochemistry and mineralogy of the alteration halo associated with the Three Crow roll-front uranium deposit, Nebraska, USA. *Mines Theses and Dissertations*, 1-173.

MacFadden, B., & Hunt, R. (1998). Magnetic polarity stratigraphy and correlation of the Arikaree Group, Arikareean (late Oligocene-early Miocene) of northwestern Nebraska. *Geological Society of America- Special Papers*, 143-166.

Martins, R. A. (1997). Becquerel and the choic of uranium compounds. *Archive for History of Exact Sciences*, 67-81.

Moreau, M., Poughon, A., Puibaraud, Y., & Sanselme, H. (1966). L'uranium et les granites. *Chron Mines Rech minere*, 47-51.

Nielsen, B., & Steenfelt, A. (1979). Intrusive events at Kvanefjeld in the Illimaussaq igneous complex. *Bulleting of Geologocial Society of Denmark*, 143-155.

Ono, S. (2001). Detrital uraninite and the early Earth's atmosphere: SIMS analyses of uraninite in the Elliot Lake district and the dissolution kinetics of natural uraninite.

Pérez, I., Casas, I., Martín, M., & Bruno, J. (2000). The thermodynamics and kinetics of uranophane dissolution in bicarbonate test solutions. *Geochimica et Cosmochimica Acta*, 603-608.

Pipiringos, G. (1955). Tertiary rocks in the central part of the Great Divide Basin, Sweetwater County, Wyoming. *10th Annual Field Conference* (pp. 100-104). Wyoming Geological Association.

Plášil, J. (2014). Oxidation-hydration weathering of uraninite: the current state-of-knowledge. *Journal of Geosciences*, 99-114.

Pollard, P. (2006). An intrusion-related orgin for Cu-Au mineralization in iron oxide-copper-gold (IOCG) provinces. *Mineralium Deposita*, 41-179.

Robie, R., & Hemingway, B. (1995). Thermodynamic properties of minerals and related substances at 298.15 K and 1 bar (10^5 pascals) pressure and at higher temperatures. *USGS*.

Ruedig, E., & Johnson, T. (2015). An evaluation of health risk to the public as a consequence of in situ uranium mining in Wyoming, USA. *Journal of environmental radioactivity*, 170-178.

Seeland, D. (1985). Seeland, D. (1985). Early Eocene paleogeography of the Bighorn Basin, northwest Wyoming, inferred from paleocurrent and particle shape and size analyses. *Geological Society of America Bulletin*.

Shock, E., & Helgeson, H. (1988). Calculation of the thermodynamic and transport properties of aqueous species at high pressures and temperatures: correlation algorithms for ionic species and equation of state predictions to 5 kb and 1000°C. *Geochimica et Cosmochimica Acta*, 2009-2036.

Shock, E., Sassani, D., Willis, M., & Sverjensky, D. (1997). Inorganic species in geologic fluids: Correlations among standard molal thermodynamic properties of aqueous ions and hydroxide complexes. *Geochimica et Cosmochimica Acta*, 907-950.

Shvareva, T., Mazeina, L., Gorman-Lewis, D., Burns, P., Szymanowski, J., Fein, J., & Navrotsky, A. (2011). Thermodynamic characterization of boltwoodite and uranophane: Enthalpy of formation and aqueous solubility. *Geochimica et Cosmochimica Acta*, 5269-5282.

Singler, C., & Picard, M. (1979). Petrography of White River group (Oligocene) in northwest Nebraska and adjacent Wyoming. *Rocky Mountain Geology* , 51-67.

Skirrow, R., Jaireth, S., Huston, D., Bastrakov, E., Schofield, A., van der Wielen, S., & Barnicoat, A. (2009). Uranium mineral systems: processes, exploration, criteria and a new deposit framework. *Geoscience Australia.*

Sørensen, J., Rose-Hansen, J., Nielsen, B., Lovborg, L., Sørensen, E., & Lundgaard, T. (1974). The uranium deposit of Kvanefjeld, the Ilimaussaq Intrusion, South Greenland. *Rapport Grønlands Geologiske Undersøgelse*, 1-55.

Stanley, K. (1976). Sandstone petrofacies in the Cenozoic High Plains sequence, eastern Wyoming and Nebraska. *Geological Society of America Bulletin*, 297-309.

Stephens, J., & Healey, D. (1964). Geology and uranium deposits at Crooks Gap, Fremont County, Wyoming. Washington, D.C.: *US Atomic Energy Commission.*

Stewart, C., Reimann, L., & Swapp, S. (2000). Mineralogic considerations for uranium in-situ leach mining: A Preliminary study of uranium and associated mineralogy of roll-front uranium deposits in Wyoming and Nebraska. *CIM Bulletin*, 89-96.

Swinehart, J., Souders, V., DeGraw, H., & Diffendal, R. (1985). Cenozoic Paleogeography of Western Nebraska. *Rocky Mountain Paleogeography Symposium 3*, 209-229.

Ur-Energy, Inc. (2016). Amended preliminary economic assessment of the Lost Creek Property Sweetwater County, Wyoming.

WNA. (2016). Supply of Uranium. Retrieved from World Nuclear Association: http://www.world-nuclear.org/information-library/nuclear-fuel-cycle/uranium-resources/supply-of-uranium.aspx

Wronkiewicz, D., Bates, J., Gerding, T., Veleckis, E., & Tani, B. (1992). Uranium release and secondary phase formation during unsaturated testing of UO2 at 90 C. *Journal of Nuclear Materials*, 107-127.

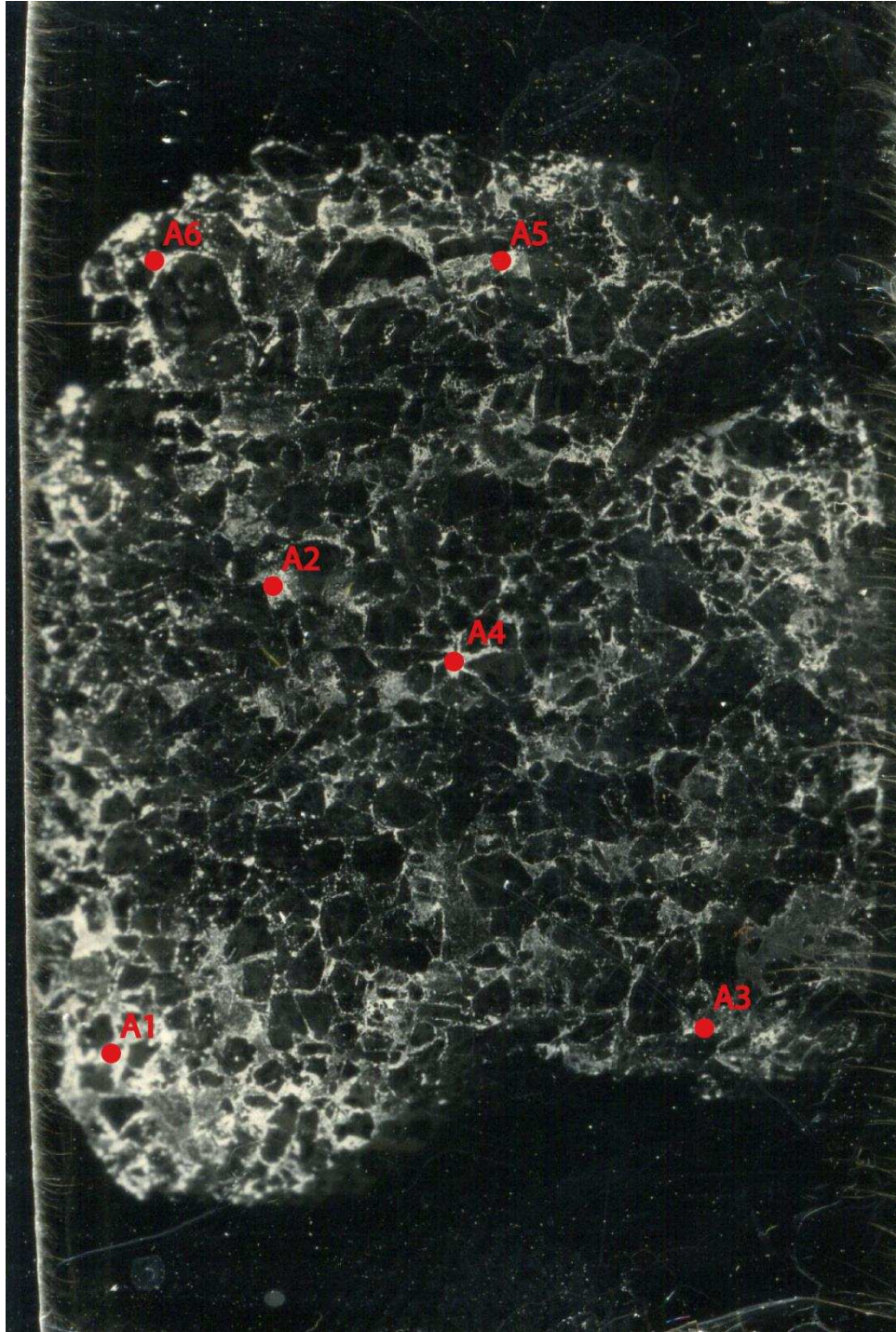Zielinski, R. (unpublished). Fission Track Mapping of U Distribution.

Figure A.1 Photograh of sample 11C: 446-447 showing the locations of the areas chosen for microprobe analysis.
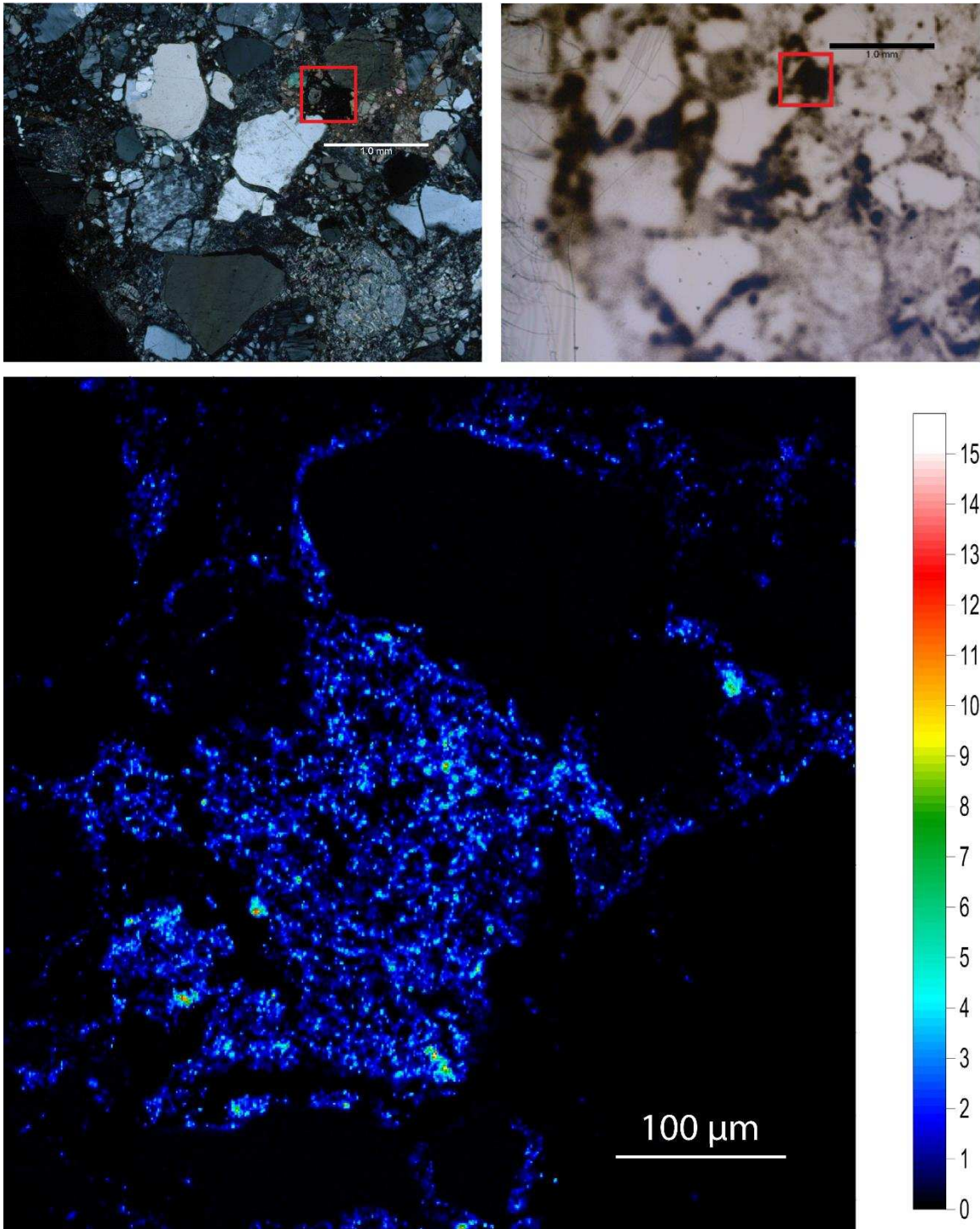
Figure A.2 Cross-polarized (top left) and plane polarized (top right) photo micrographs of point A1 from sample 11C: 446-447 showing areas selected for EMPA analysis in the red box. Results from the microprobe analysis (bottom) with scale in wt. % U.
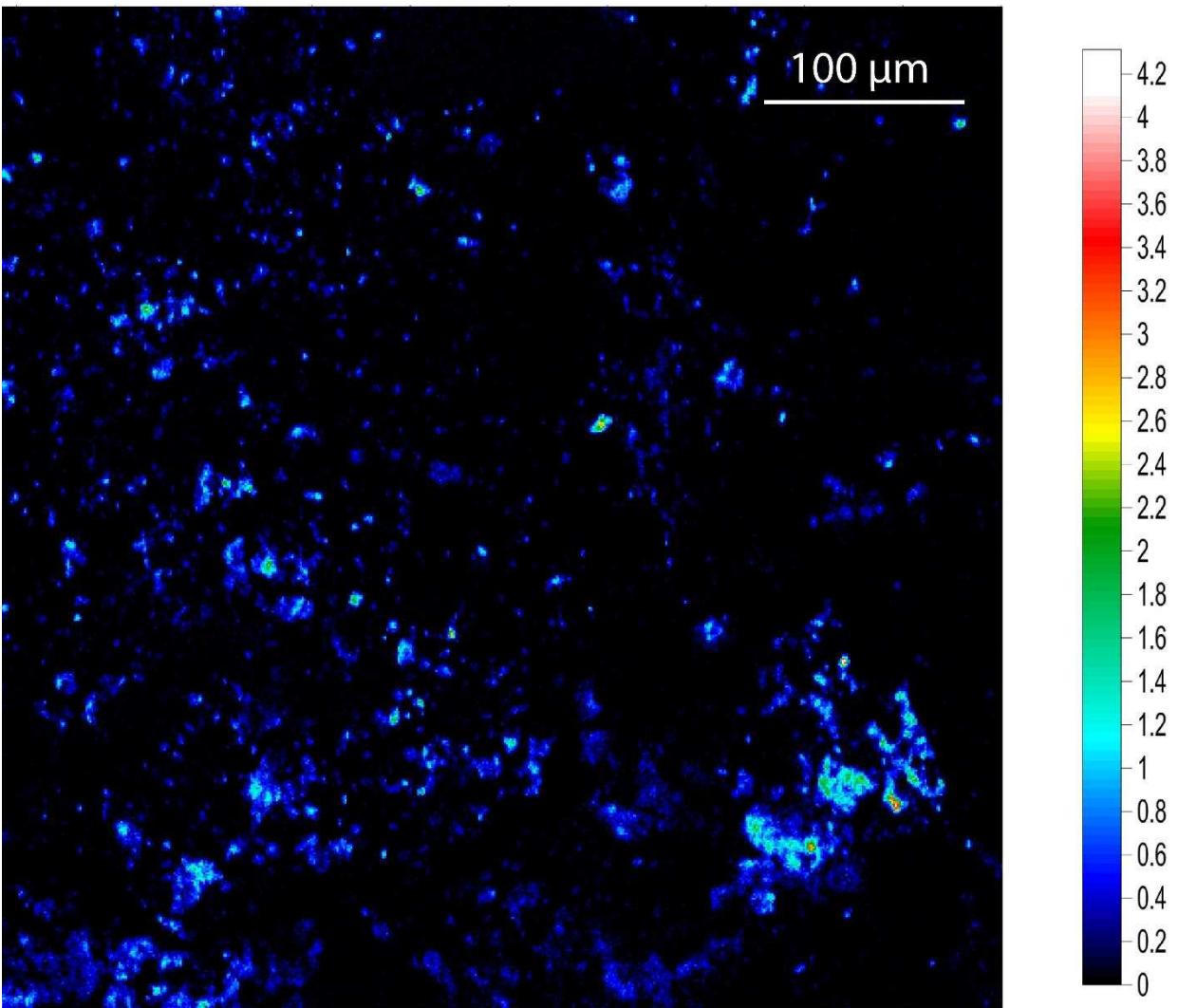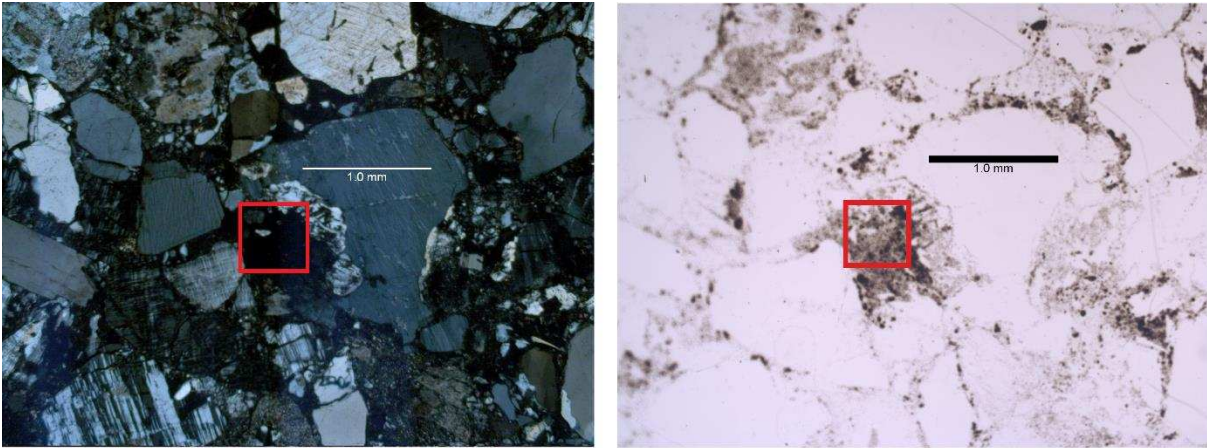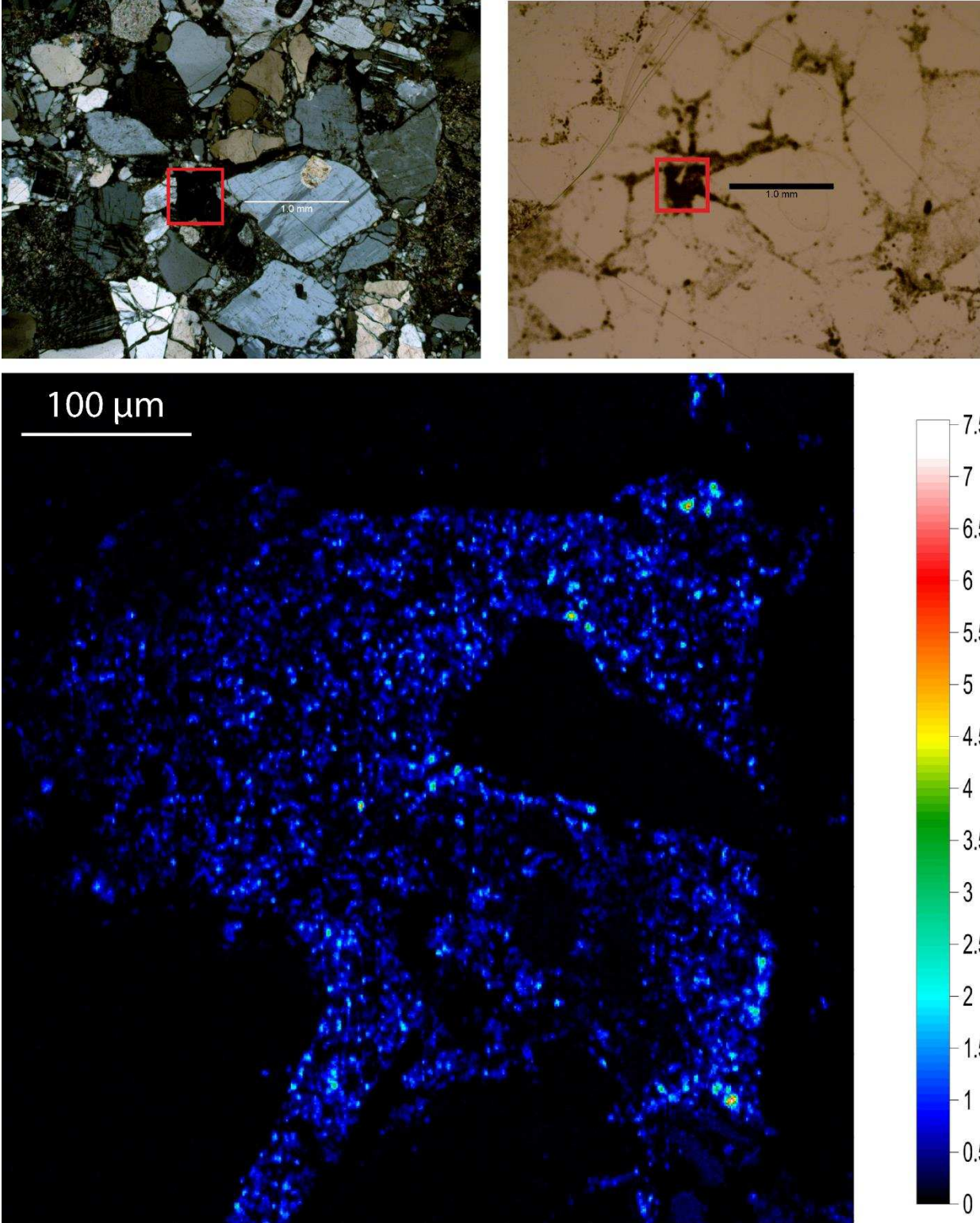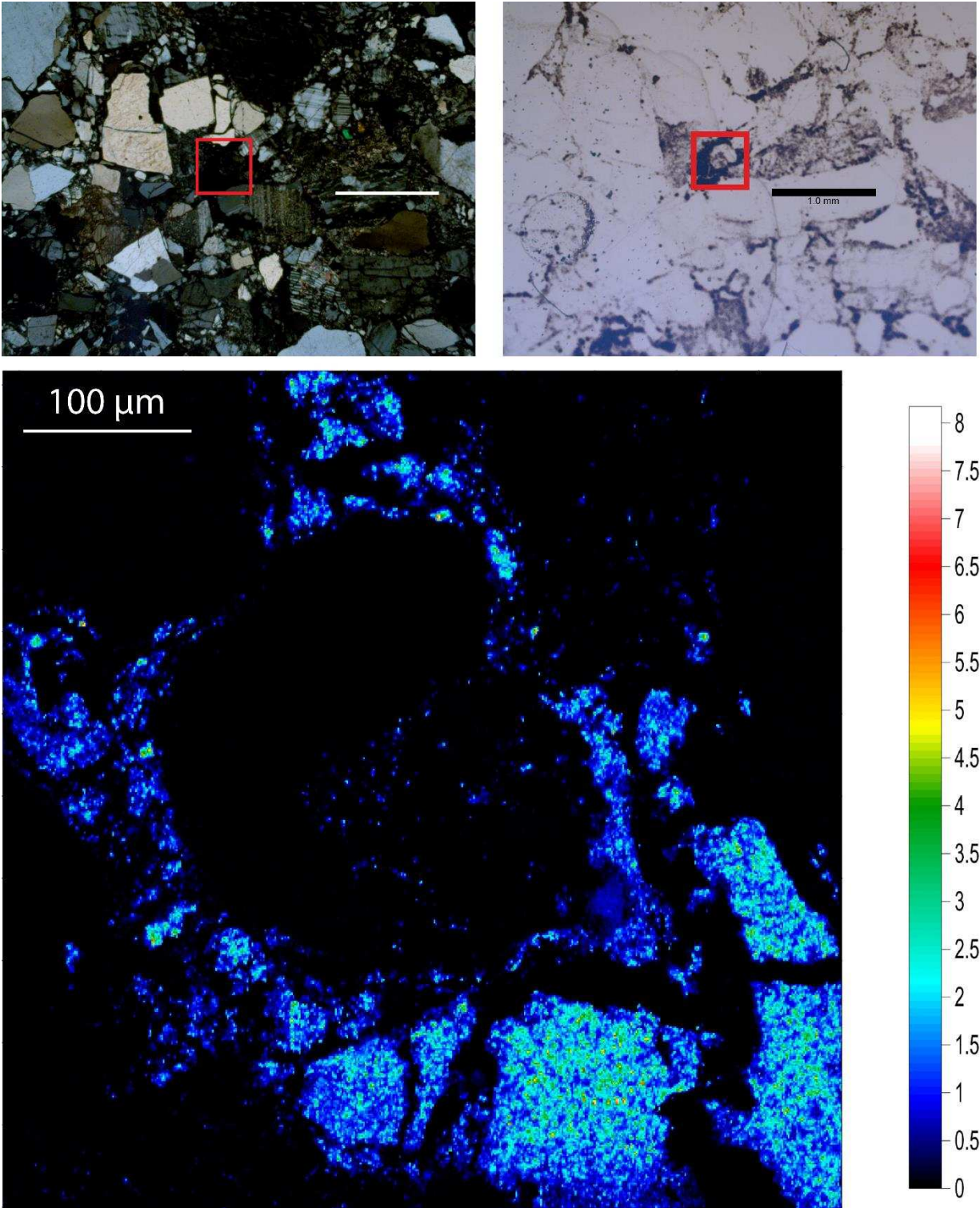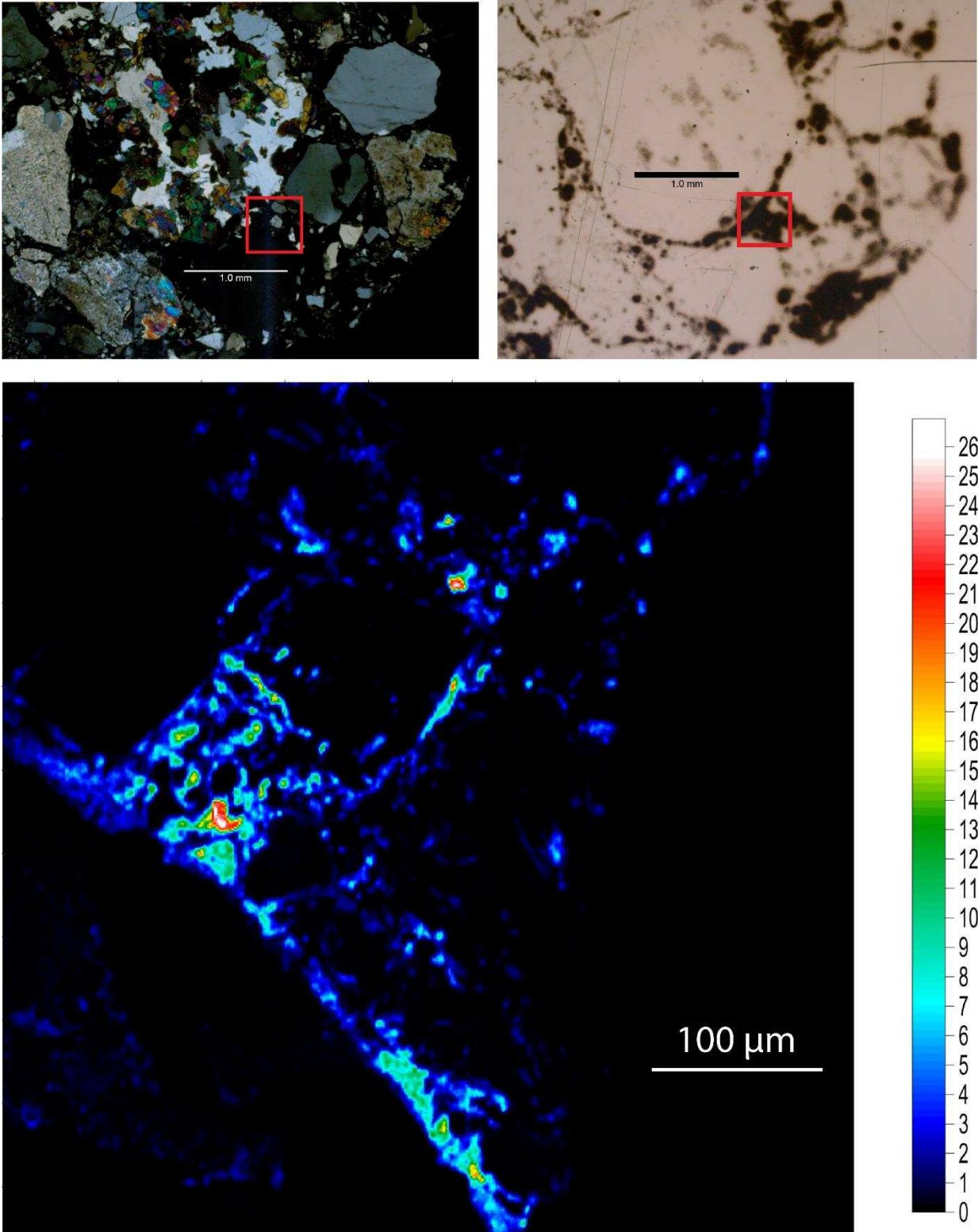
Figure A.3 Cross-polarized (top left) and plane polarized (top right) photo micrographs of point A2 from sample 11C: 446-447 showing areas selected for EMPA analysis in the red box. Results from the microprobe analysis (bottom) with scale in wt. % U.
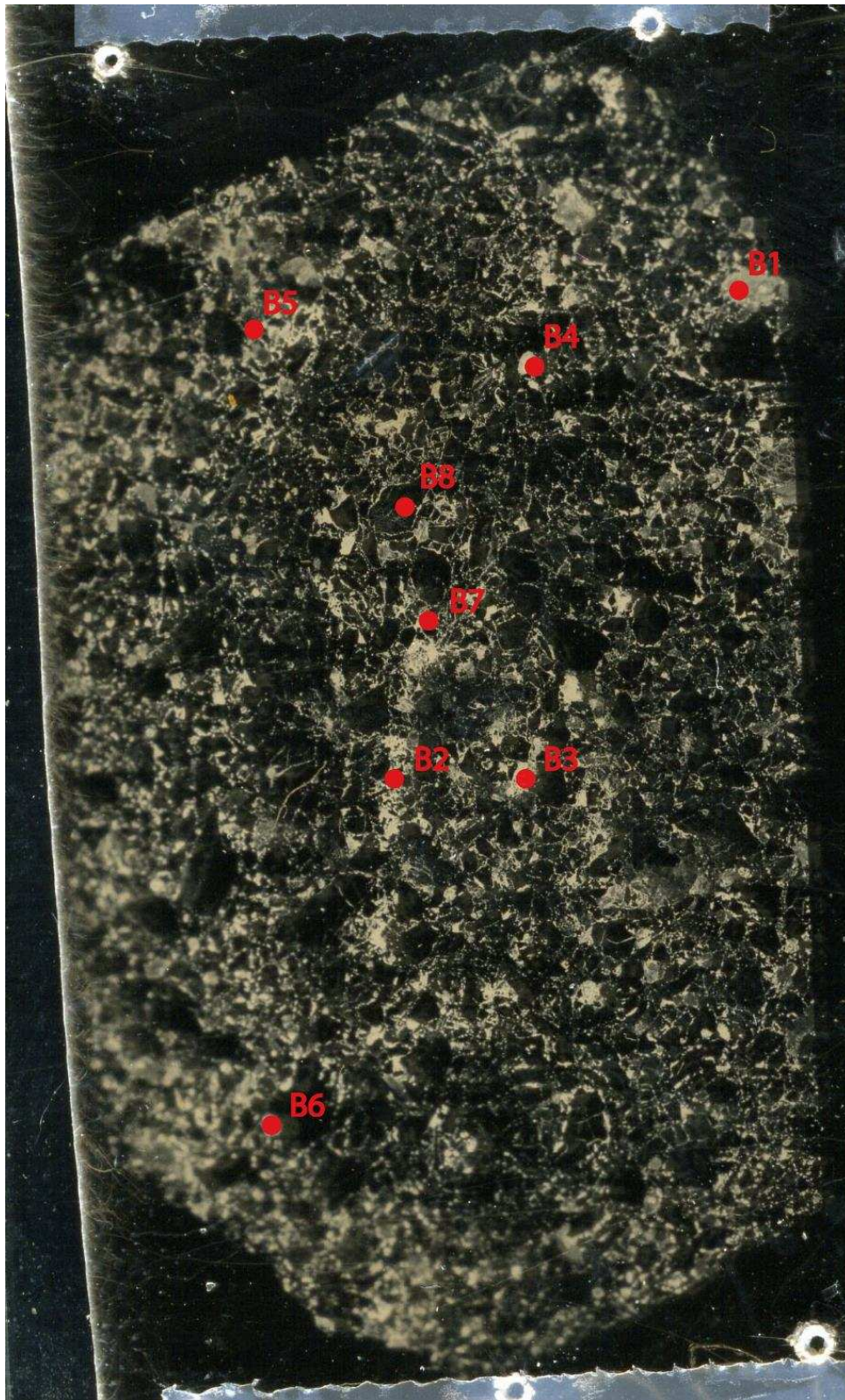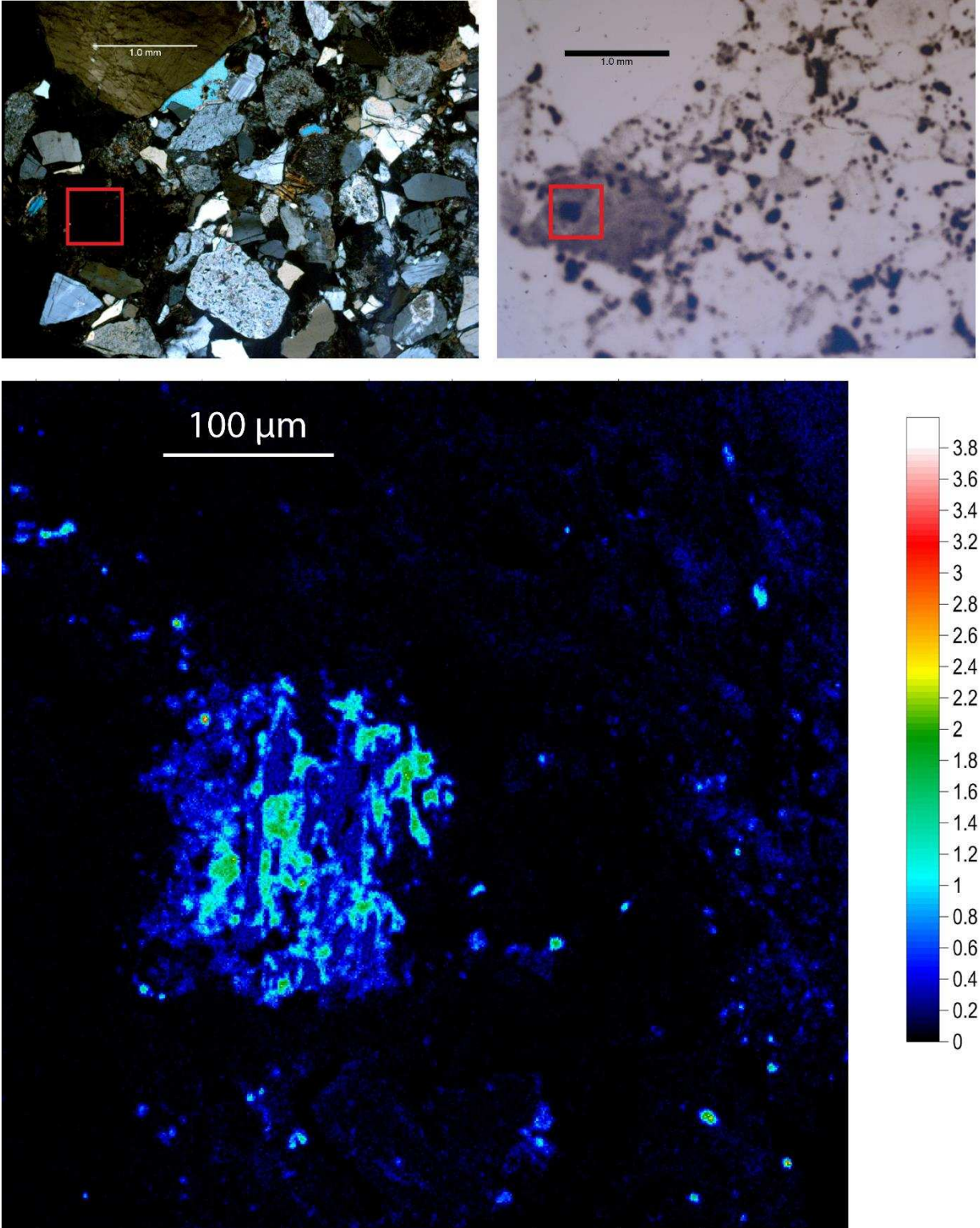
Figure A.4 Cross-polarized (top left) and plane polarized (top right) photo micrographs of point A4 from sample 11C: 446-447 showing areas selected for EMPA analysis in the red box. Results from the microprobe analysis (bottom) with scale in wt. % U.

Figure A.5 Cross-polarized (top left) and plane polarized (top right) photo micrographs of point A5 from sample 11C: 446-447 showing areas selected for EMPA analysis in the red box. Results from the microprobe analysis (bottom) with scale in wt. % U.
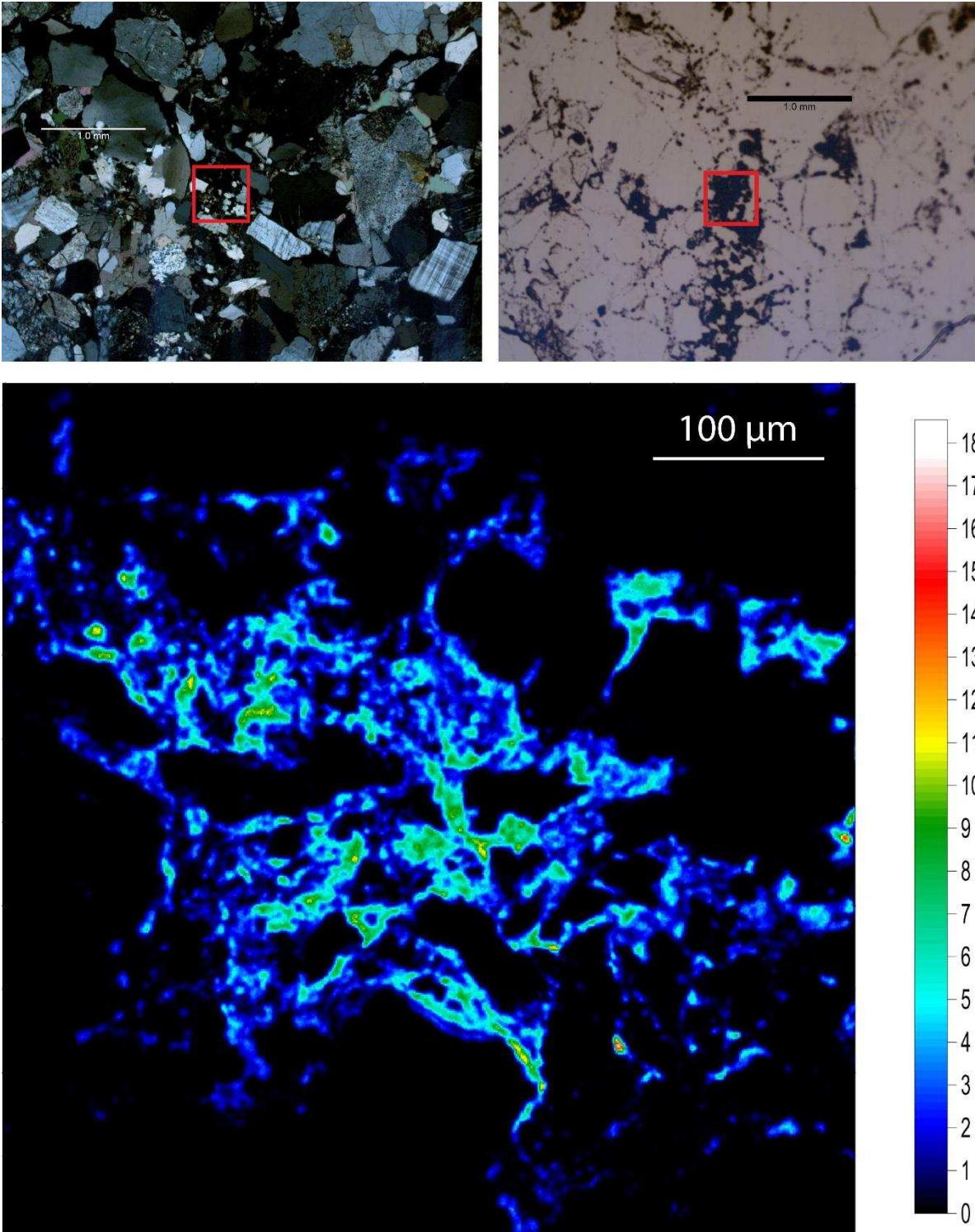
Figure A.6 Cross-polarized (top left) and plane polarized (top right) photo micrographs of point A6 from sample 11C: 446-447 showing areas selected for EMPA analysis in the red box. Results from the microprobe analysis (bottom) with scale in wt. % U.

Figure A.7 Photograh of sample 13C: 412-413 showing the locations of the areas chosen for microprobe analysis.

Figure A.8 Cross-polarized (top left) and plane polarized (top right) photo micrographs of point B1 from sample 13C: 412-413 showing areas selected for EMPA analysis in the red box. Results from the microprobe analysis (bottom) with scale in wt. % U.
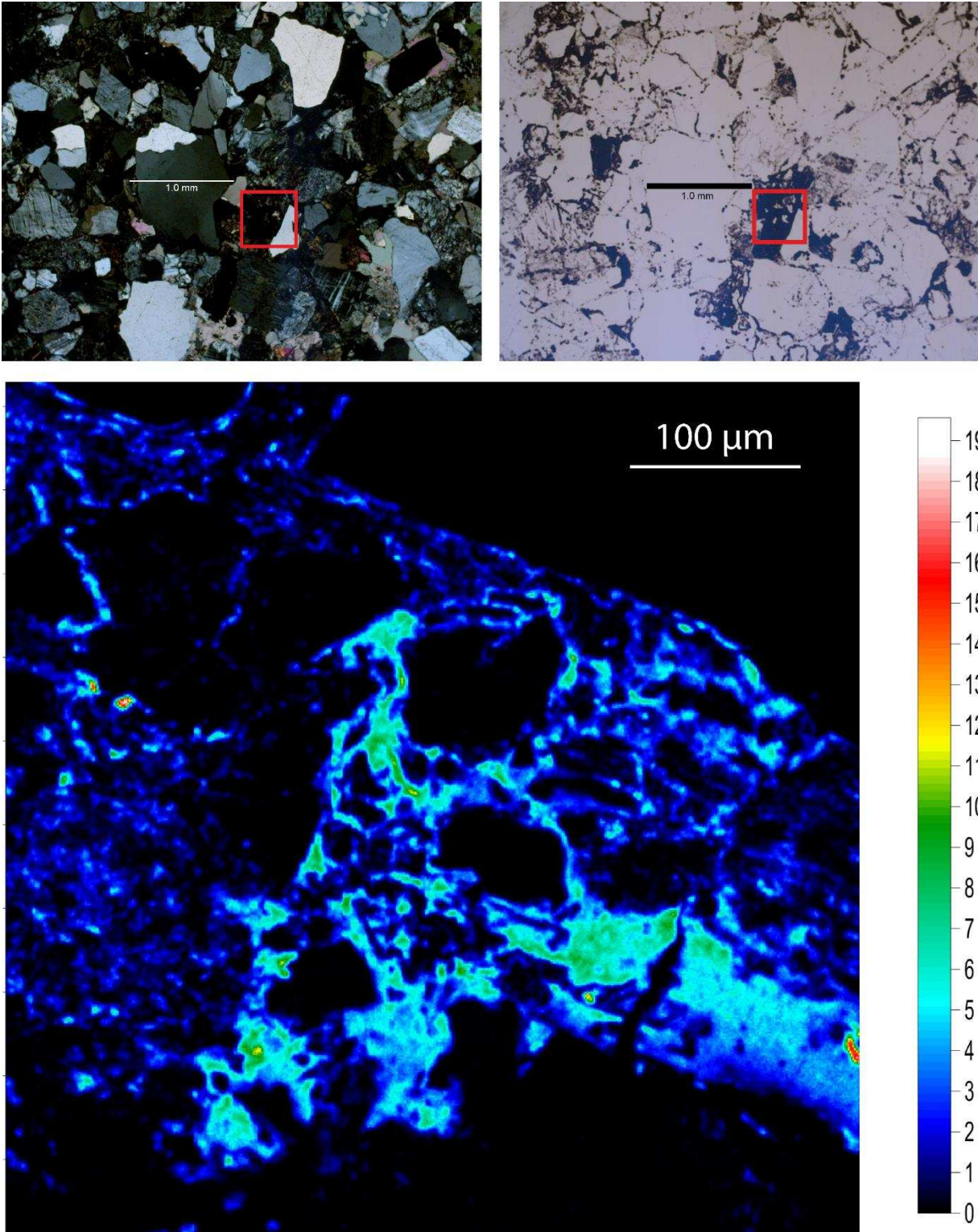
Figure A.9 Cross-polarized (top left) and plane polarized (top right) photo micrographs of point B2 from sample 13C: 412-413 showing areas selected for EMPA analysis in the red box. Results from the microprobe analysis (bottom) with scale in wt. % U.
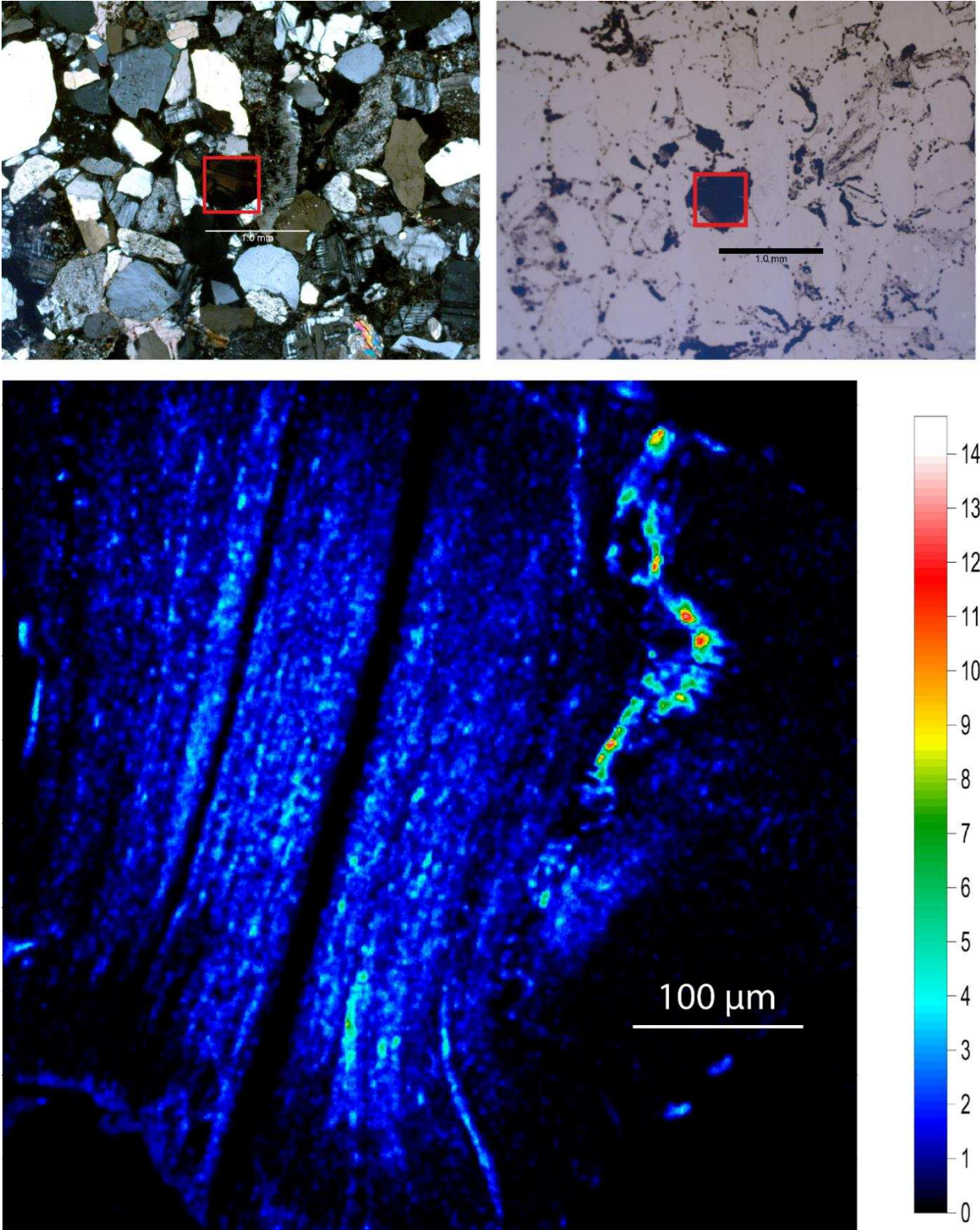
Figure A.10 Cross-polarized (top left) and plane polarized (top right) photo micrographs of point B3 from sample 13C: 412-413 showing areas selected for EMPA analysis in the red box. Results from the microprobe analysis (bottom) with scale in wt. % U.
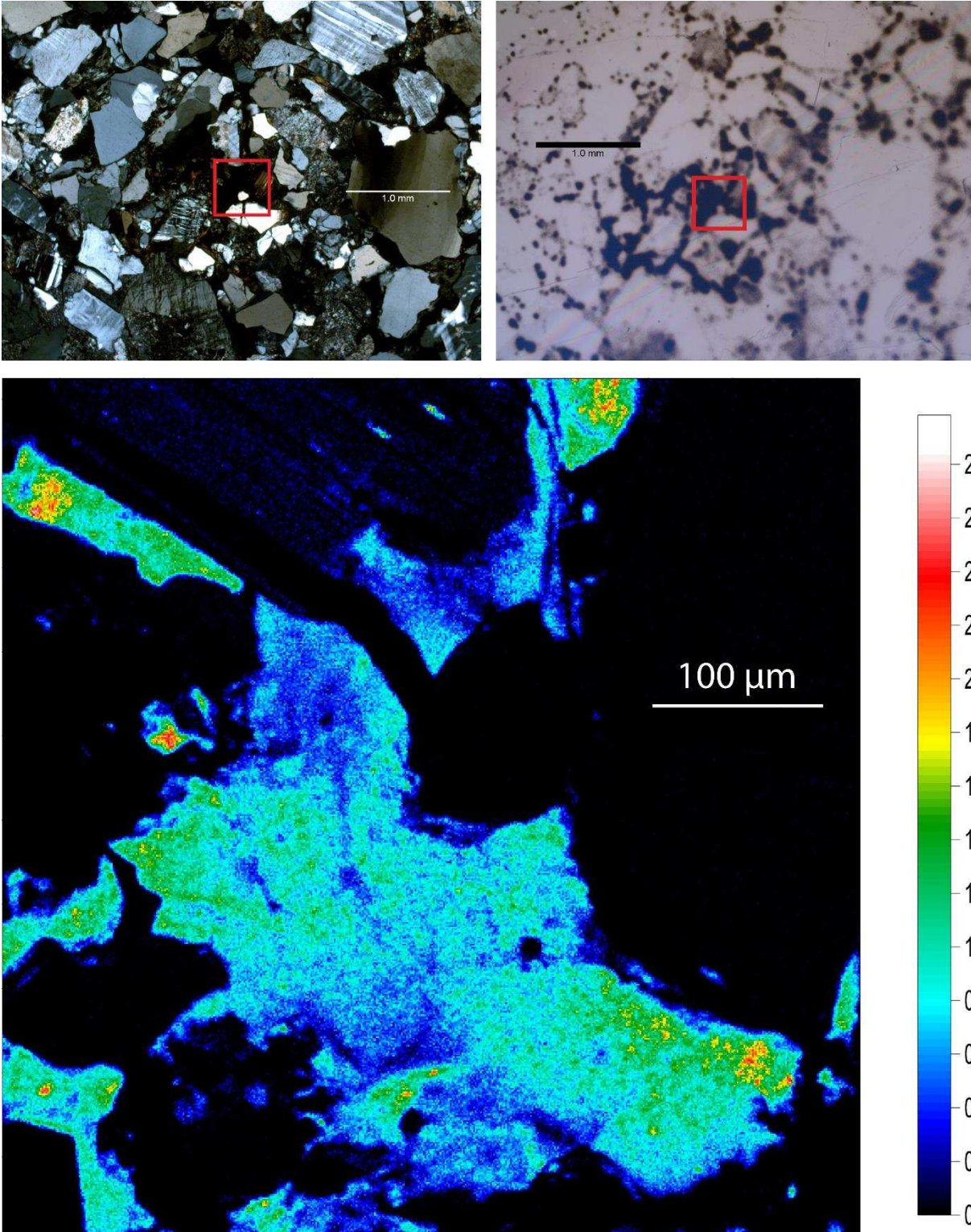
Figure A.11 Cross-polarized (top left) and plane polarized (top right) photo micrographs of point B4 from sample 13C: 412-413 showing areas selected for EMPA analysis in the red box. Results from the microprobe analysis (bottom) with scale in wt. % U.

Figure A.12 Cross-polarized (top left) and plane polarized (top right) photo micrographs of point B5 from sample 13C: 412-413 showing areas selected for EMPA analysis in the red box. Results from the microprobe analysis (bottom) with scale in wt. % U.
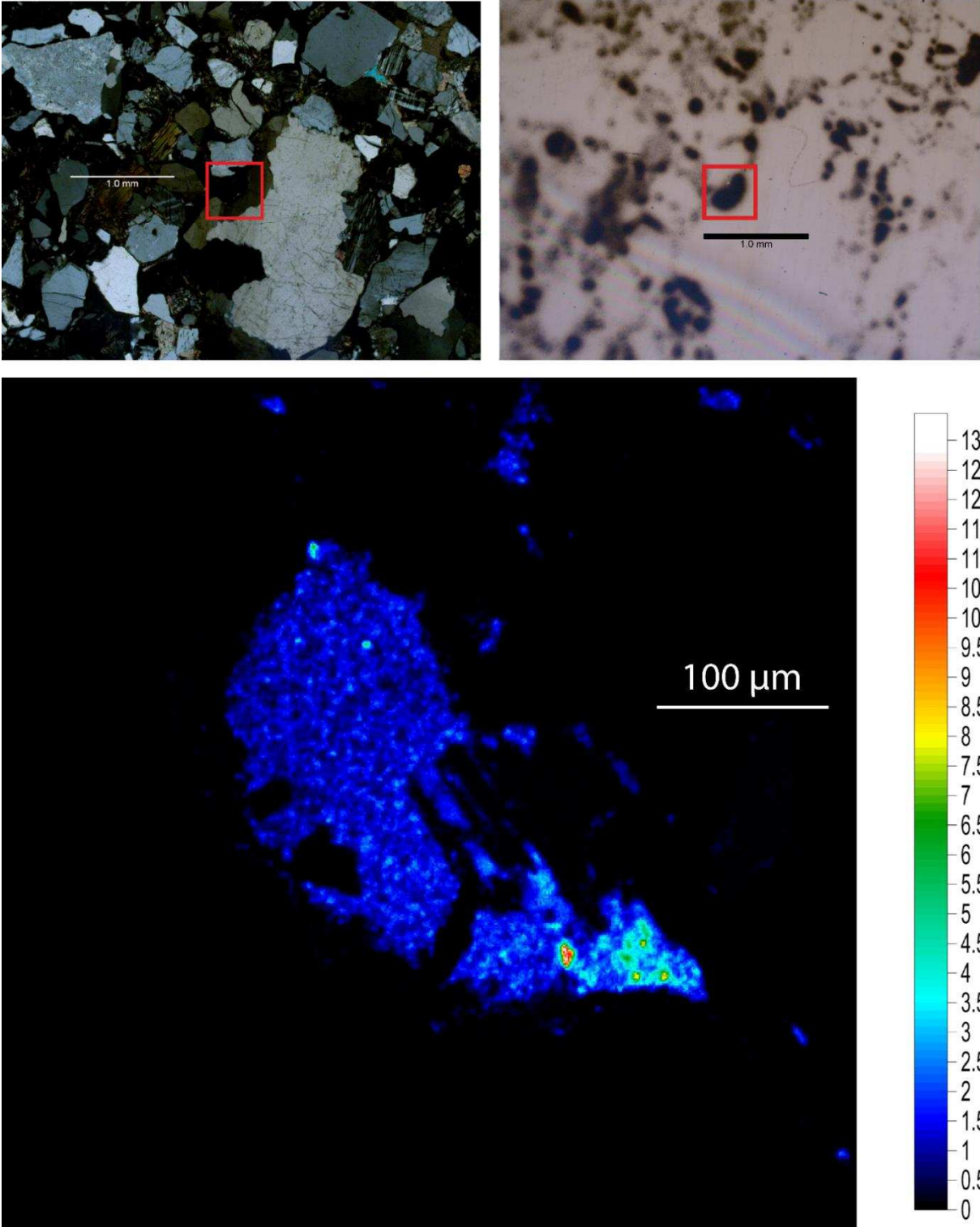
Figure A.13 Cross-polarized (top left) and plane polarized (top right) photo micrographs of point B6 from sample 13C: 412-413 showing areas selected for EMPA analysis in the red box. Results from the microprobe analysis (bottom) with scale in wt. % U.
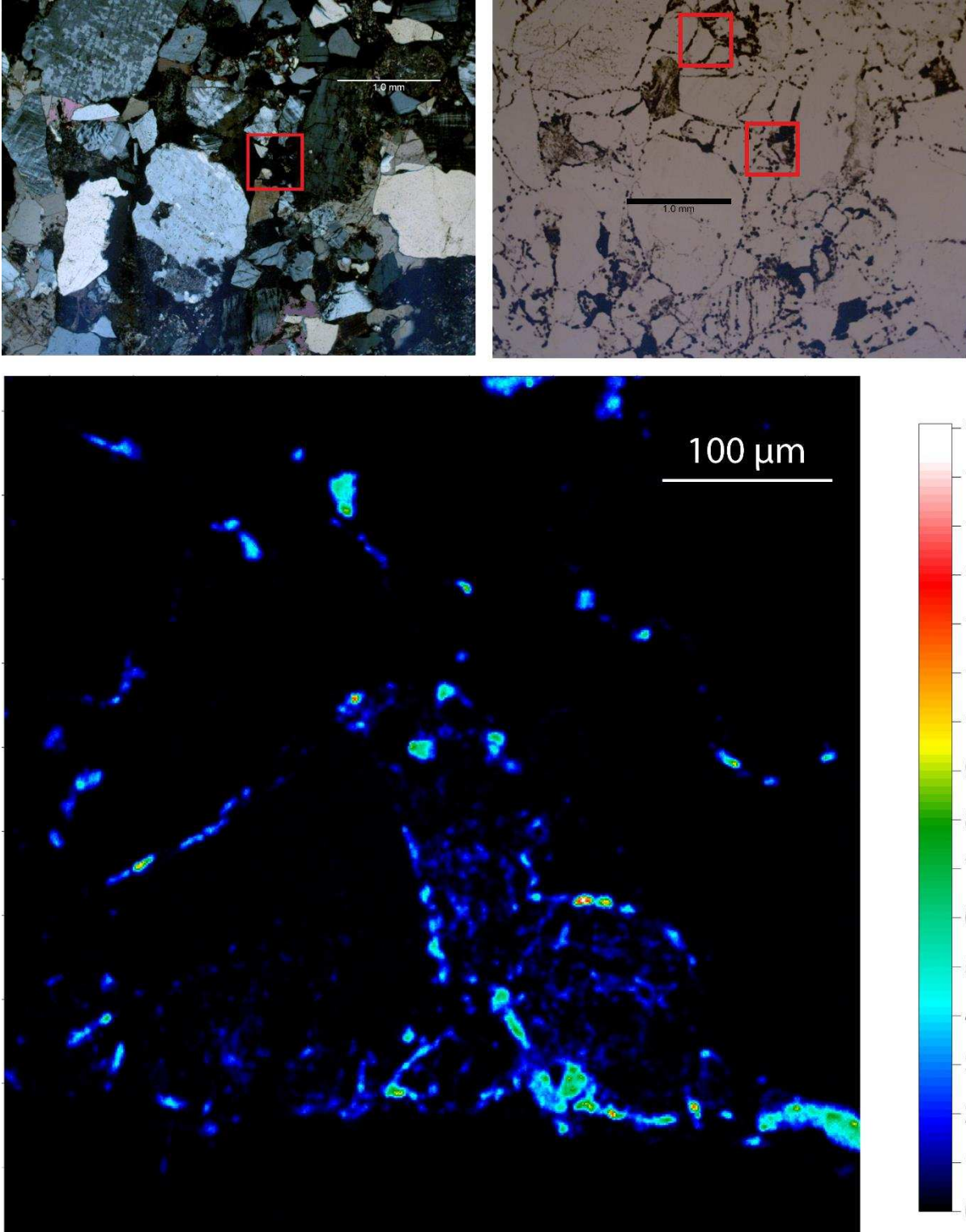
Figure A.14 Cross-polarized (top left) and plane polarized (top right) photo micrographs of point B7 from sample 13C: 412-413 showing areas selected for EMPA analysis in the red box. Results from the microprobe analysis (bottom) with scale in wt. % U.
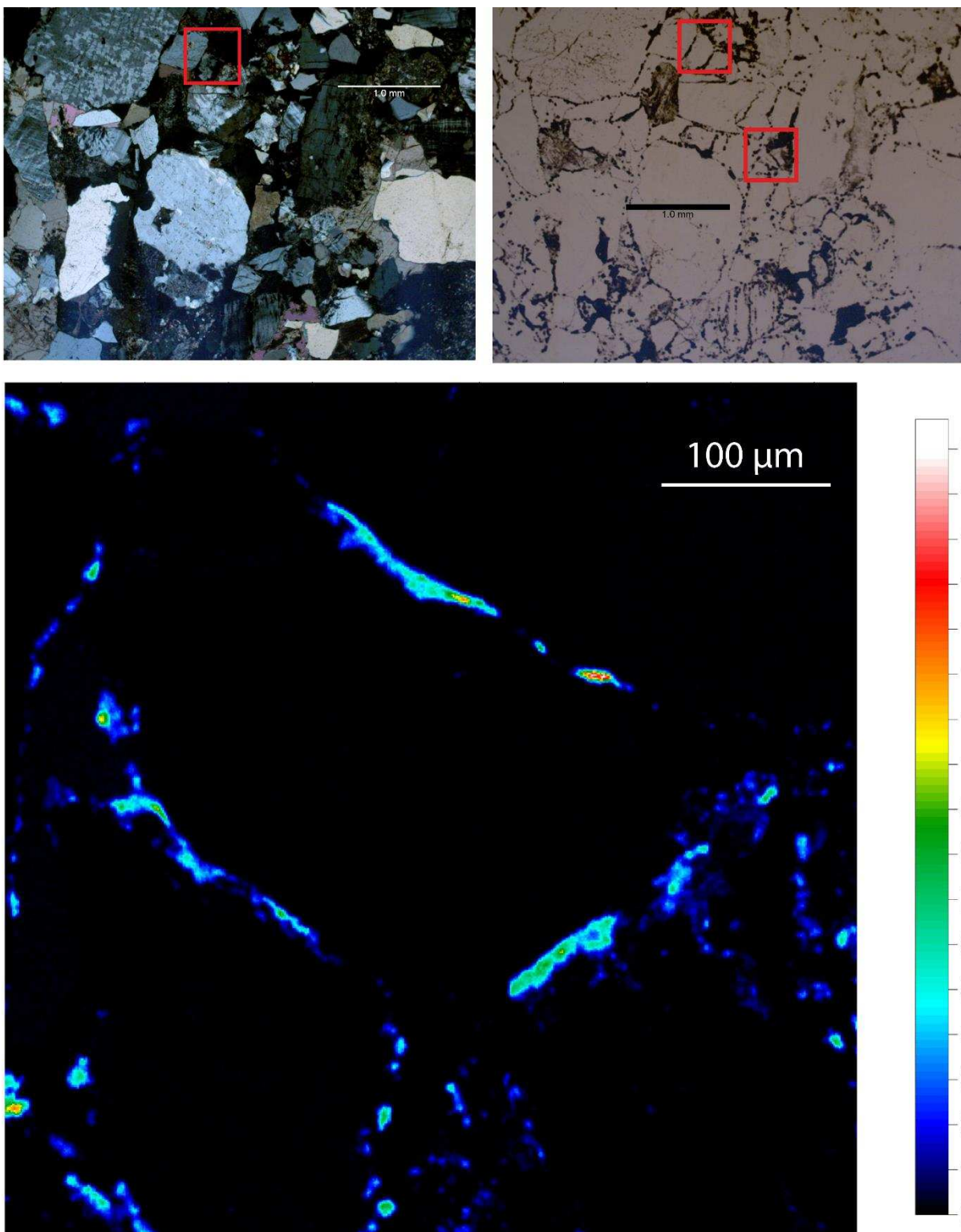
Figure A.15 Cross-polarized (top left) and plane polarized (top right) photo micrographs of point B8 from sample 13C: 412-413 showing areas selected for EMPA analysis in the red box. Results from the microprobe analysis (bottom) with scale in wt. % U.